

Infrasound Emitted by Tornado-Like Vortices: Basic Theory and a Numerical Comparison to the Acoustic Radiation of a Single-Cell Thunderstorm

DAVID A. SCHECTER

NorthWest Research Associates, Redmond, Washington

MELVILLE E. NICHOLLS

Cooperative Institute for Research in Environmental Sciences, University of Colorado, Boulder, Colorado

JOHN PERSING

Department of Mathematics, Colorado State University, Fort Collins, Colorado

ALFRED J. BEDARD JR.

Cooperative Institute for Research in Environmental Sciences, University of Colorado, and National Oceanic and Atmospheric Administration/Earth System Research Laboratory, Boulder, Colorado

ROGER A. PIELKE SR.

Cooperative Institute for Research in Environmental Sciences, University of Colorado, Boulder, Colorado

(Manuscript received 28 December 2006, in final form 28 May 2007)

ABSTRACT

This paper addresses the physics and numerical simulation of the adiabatic generation of infrasound by tornadoes. Classical analytical results regarding the production of infrasound by vortex Rossby waves and by corotating “suction vortices” are reviewed. Conditions are derived for which critical layers damp vortex Rossby waves that would otherwise grow and continually produce acoustic radiation. These conditions are similar to those that theoretically suppress gravity wave radiation from larger mesoscale cyclones, such as hurricanes. To gain perspective, the Regional Atmospheric Modeling System (RAMS) is used to simulate the infrasound that radiates from a single-cell thunderstorm in a shear-free environment. In this simulation, the dominant infrasound in the 0.1–10-Hz frequency band appears to radiate from the vicinity of the melting level, where diabatic processes involving hail are active. It is shown that the 3D Rossby waves of a tornado-like vortex (simulated with RAMS) can generate stronger infrasound if the maximum wind speed of the vortex exceeds a modest threshold. Technical issues regarding the numerical simulation of tornado infrasound are also addressed. Most importantly, it is shown that simulating tornado infrasound likely requires a spatial resolution that is an order of magnitude finer than the current practical limit (10-m grid spacing) for modeling thunderstorms.

1. Introduction

Recent field experiments in the high plains of the United States indicate that tornadic thunderstorms emit infrasound at frequencies between 0.1 and 10 Hz much more intensely than nonsevere weather systems (Bedard 2005; Bedard et al. 2004; Szoke et al. 2004). The unsteady motion of a developing or mature tornado is one likely source of the relatively strong signal

(ibid.; Georges 1976; Passner and Noble 2006). Based on this hypothesis, the Physical Sciences Division of the Earth Systems Laboratory and the National Weather Service Forecast Offices of the National Oceanic and Atmospheric Administration (NOAA) are evaluating the use of infrasound detection for tornado warning.¹

In principle, tornadoes can exhibit very complex fluctuations that produce equally complex acoustic radia-

Corresponding author address: David Schecter, NorthWest Research Associates, 4118 148th Ave. NE, Redmond, WA 98052.
E-mail: schecter@nwra.com

¹ The preliminary evaluation by NOAA has concluded since this article was submitted for publication. The results are quite promising, and are currently summarized online. (<http://www.esrl.noaa.gov/psd/programs/infrasound/isnet/>).

tion fields. In order to build a foundation for understanding tornado infrasound, previous studies have assessed the importance of relatively simple mechanisms for its generation. Basic sources of tornado infrasound include axisymmetric (radial) vibrations, the corotation of suction vortices, and turbulence in the vortex boundary layer. Recent estimates put the typical frequency of boundary layer turbulence and its acoustic radiation field above the observational cutoff (Bedard 2005). Moreover, the infrasound of severe storms often seems to originate from aloft (*ibid.*). In principle, a sufficient number of corotating suction vortices can produce infrasound in the pertinent 0.1–10-Hz frequency band. So too can radial vibrations (*ibid.*; Abdullah 1966). Indeed, Bedard et al. (2004) and Bedard (2005) show that radial vibrations might best account for their particular observations.

Conceivably, vortex Rossby waves represent another basic source of acoustic radiation that can produce spectral peaks in tornado infrasound. Vortex Rossby waves owe their existence to the radial gradient of basic-state axial vorticity. They are positively coupled to their acoustic radiation fields, which leads to amplification under ideal conditions (e.g., Kop'ev and Lent'ev 1983, 1985, 1988; Zeitlin 1991). As explained below, this paper provides evidence that the Rossby waves of a tornado can be stronger sources of infrasound than an entire single-cell thunderstorm. Whether or not the infrasound of a vortex Rossby wave can exceed the background noise of an organized supercell is an issue that is left for future research.

In the absence of detailed observations, numerical modeling may provide the best method for analyzing the generation of infrasound in a tornadic thunderstorm. Ideally, realistic simulations would reveal a comprehensive set of conditions under which tornadoes emit infrasound at greater intensity than other flow structures or diabatic cloud processes. Furthermore, realistic simulations would clarify the favored mechanisms by which tornadoes produce infrasound in the observational frequency band.

In this paper, we examine the viability of the fully compressible Regional Atmospheric Modeling System (RAMS; Cotton et al. 2003; Medvigy et al. 2005) for simulating the infrasound of a tornadic thunderstorm. Previous studies have established that RAMS can create thunderstorms that spawn tornadoes (Grasso and Cotton 1995; Pielke et al. 1995; Finley et al. 2001). Here, we further establish that RAMS can adequately simulate aeroacoustic phenomena. Specifically, we compare two classical analytical theories of vortex sound to two sets of experiments with RAMS. The first

theory pertains to spiral acoustic radiation that is generated by the Rossby waves of a 2D homentropic (uniform enstrophy) Rankine vortex. The second theory pertains to the spiral radiation that is generated by a 2D ring of corotating suction vortices. At sufficiently high spatial resolution, and where applicable, there is good agreement between theory and RAMS. Following this verification, we use RAMS to simulate the infrasound that is produced by the Rossby waves of a 3D tornado-like vortex of variable intensity.

The very fine spatial resolution (of the order of 1-m grid spacing) that is required to accurately simulate tornado infrasound is currently impractical for modeling full thunderstorms. Nevertheless, we provisionally use RAMS at coarser resolution (30-m grid spacing) to simulate the acoustic radiation of a nontornadic thunderstorm in a shear-free environment. The dominant component of the thunderstorm radiation, in the 0.1–10-Hz frequency band, appears to emanate from the vicinity of the melting level, where diabatic processes involving hail are active. Section 5 compares the thunderstorm radiation to that of model tornadoes with Mach numbers between 0.1 and 0.3. It is shown that the model tornadoes can produce 0.1–10-Hz infrasound either at or above the simulated thunderstorm noise, via Rossby waves of modest amplitudes.

Given our emphasis on the potential importance of vortex Rossby waves, it is appropriate to discuss conditions that inhibit their production of infrasound. To this end, we appeal to the analogous theory of gravity wave radiation by vortex Rossby waves in mesoscale cyclones, such as hurricanes. Schechter and Montgomery (2004, 2006, 2007) recently derived conditions for which critical layers within a mesoscale cyclone can damp its Rossby waves and thereby suppress the radiation of spiral gravity waves. To conclude this paper, we derive similar conditions that allow critical layers to suppress the production of infrasound by the Rossby waves of a tornado.

Briefly, this paper is organized as follows. Section 2 reviews basic elements of the theory of acoustic radiation from vortical flows. Section 3 compares 2D analytical theories of vortex infrasound to RAMS simulations. In addition, section 3 examines a RAMS simulation of acoustic radiation from a 3D tornado-like vortex whose intensity decays with height. Section 4 examines radiation from a simulated nontornadic thunderstorm. Section 5 compares the simulated thunderstorm radiation to the simulated infrasound of a 3D vortex. Section 5 also discusses the potential importance of vortex infrasound toward explaining the observed acoustic signatures of severe weather systems. Section 6 presents

the analogy between acoustic radiation from tornado-like vortices and gravity wave radiation from hurricane-like vortices via vortex Rossby waves. Section 7 recapitulates our conclusions. The appendixes provide various technical details for those interested in reproducing and extending the results that are presented in the main text.

2. Basic theory of vortex sound

a. 3D Lighthill radiation

Lighthill (1952) derived the following estimate for the acoustic radiation field that is generated by a three-dimensional compact region of “turbulence” in a homentropic fluid:

$$p' \sim \rho_o c_o^2 M^4 \frac{L}{|\mathbf{x}|}. \tag{1}$$

Here, p' is the pressure perturbation, ρ_o is the ambient mass density, c_o is the ambient sound speed, L is the length scale of the turbulent source, and $|\mathbf{x}|$ is distance from the source. The Mach number M is defined by

$$M \equiv \frac{V}{c_o}, \tag{2}$$

in which V is the characteristic velocity of the turbulence. Although Lighthill did not emphasize the connection between acoustic radiation and motion of vorticity within the turbulence, this connection is essential to the theoretical framework that was later developed by Powell (1964). For comprehensive reviews of the theory of “vortex sound,” the reader may consult Howe (2003), Aurégan et al. (2002), and Lyamshev and Skvortsov (1988).

It is important to note that Eq. (1) was derived under the assumptions that the turbulence is highly subsonic ($M \ll 1$), that the fluid is unbounded, and that the fluid is homentropic. The Mach number scaling can vary appreciably with boundary conditions, entropy inhomogeneities, and heat release by chemical reactions or phase transitions within the fluid. Equation (1) serves merely to illustrate that acoustic radiation from unembellished low Mach number flows can be fairly weak. Below (section 5) we will discuss its detectability in greater detail.

b. Radiation from a 2D Rankine vortex

In this and the following subsection, we shall consider two paradigms of vortex sound. The first paradigm is for acoustic radiation that is generated by the Rossby waves of a two-dimensional Rankine vortex

(see Fig. 5). The basic state of a Rankine vortex consists of an interior and an exterior region. The interior region is in solid body rotation. The exterior region consists of a tangential velocity field that decays inversely with radius. Specifically,

$$\bar{v} = \begin{cases} Vr/R, & r \leq R, \\ VR/r, & r > R, \end{cases} \tag{3}$$

in which V is the maximum wind speed and R is the radius of maximum wind.

Alternatively, one may view the Rankine vortex as a uniform circular vortex patch of radius R and vorticity $2V/R$. The discrete Rossby waves of a Rankine vortex are disturbances of the circular boundary that propagate azimuthally in the same direction of the flow, but at a phase speed less than V .

At low rotational Mach numbers, $M = V/c_o \ll 1$, we may treat the vortex motion as incompressible. In the incompressible limit, the dispersion relation for discrete vortex Rossby waves (e.g., Kelvin 1880) is given by

$$\omega_n = \Omega(n - 1), \tag{4}$$

in which $n \geq 2$ is the azimuthal wavenumber, ω_n is the angular frequency of the wave, and $\Omega \equiv V/R$.²

At distances $r \geq R/M$, incompressibility becomes a poor approximation. As r increases toward this region, the pressure perturbation of the Rossby wave matches onto an outward propagating spiral sound wave. The asymptotic form of the pressure perturbation, valid for $r \gg c_o/\omega_n$, is given by Howe (1975) and Broadbent (1976):

$$p_n \approx \sqrt{\frac{8\pi R}{r}} \epsilon \rho_o c_o^2 M^{n+3/2} \frac{(n - 1)^{n+1/2}}{n! 2^{n+1}} \times \cos[n\phi + r\omega_n/c_o - \omega_n t - (2n - 1)\pi/4]. \tag{5}$$

Here, ϵ is the dimensionless Rossby wave amplitude, that is, the maximal radial displacement of the outer edge of the vortex patch, normalized to R .

Kop’ev and Leont’ev (1983) further showed that the acoustic radiation has positive feedback on a Rossby wave, causing it to grow at the following rate:

$$\gamma_n = \frac{\pi n(n - 1)^{2n}}{(n!)^2 2^{2n}} M^{2n} \Omega. \tag{6}$$

² Here, we have assumed that the mass density is uniform in the incompressible limit. Howe (1977) demonstrates that a density jump between the environment and the vortex core permits a discrete normal mode with $n = 1$ and $\omega_n \neq 0$.

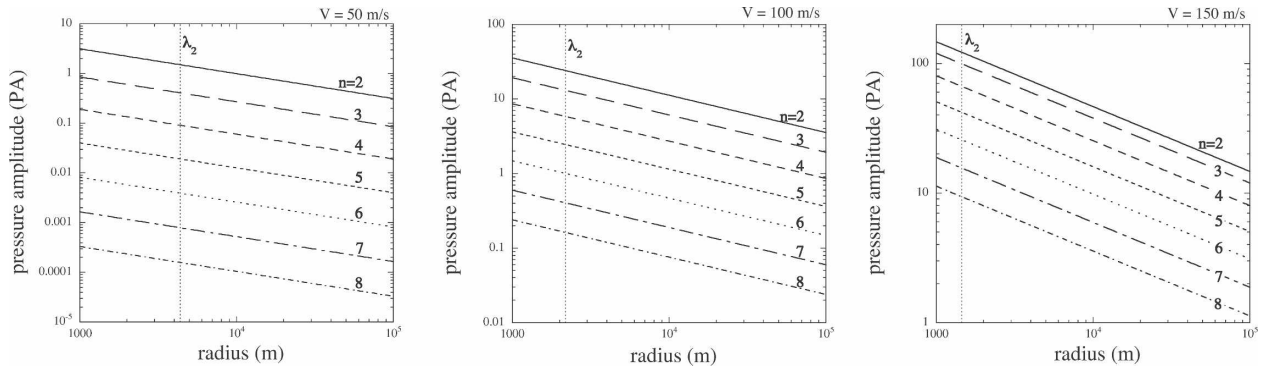


FIG. 1. Low Mach number theory [Eq. (5)] for the peak-to-peak amplitude of an outward-propagating spiral acoustic wave that is generated by a discrete mode (Rossby wave) of a 2D Rankine vortex for (left) $V = 50$, (middle) $V = 100$, and (right) $V = 150 \text{ m s}^{-1}$. As shown, the amplitude of the spiral wave decreases as 1) r increases, 2) n increases, and 3) V decreases. All amplitudes are calculated with $\epsilon = 0.1$, $R = 100 \text{ m}$, $c_o = 347.2 \text{ m s}^{-1}$, and $\rho_o = 1.16 \text{ kg m}^{-3}$. The dashed vertical line in each plot indicates the maximum radial wavelength (λ_2) of the spiral radiation. In principle, the plotted theory is inaccurate for $r < \lambda_n$.

Equations (5) and (6) are derived in appendixes A and B for the benefit of readers who are unfamiliar with this material.

Note that the growth rate γ_n vanishes rapidly with Mach number and is quite small for tornadic parameters. For example, if $V \leq 100 \text{ m s}^{-1}$, $R \geq 100 \text{ m}$, and $c_o = 347.2 \text{ m s}^{-1}$, then $\gamma_n \leq 7 \times 10^{-4} \text{ s}^{-1}$. In other words, the Rossby waves would have e -folding times that exceed 24 min. Nevertheless, their initial amplitudes, which are determined by the degree of asymmetry during tornado genesis or by an asymmetric impulse, can suffice to produce measurable radiation.

Figure 1 shows the peak-to-peak amplitude of the radiation pressure field [Eq. (5)] as a function of radius for vortices with $R = 100 \text{ m}$ and $V = 50 \text{ m s}^{-1}$, 100 m s^{-1} , and 150 m s^{-1} . For all cases, the ambient sound speed is $c_o = 347.2 \text{ m s}^{-1}$, corresponding to ambient pressure $p_o = 10^5 \text{ Pa}$, ambient density $\rho_o = 1.16 \text{ kg m}^{-3}$, and the ratio of specific heats $C_p/C_v \approx 1.40$. Figures 2a,b show the frequency and asymptotic radial wavelength,

$$f_n \equiv \frac{\omega_n}{2\pi} \quad \text{and} \quad \lambda_n \equiv 2\pi c_o / \omega_n, \quad (7)$$

of the radiation field versus azimuthal wavenumber n . All Rossby waves with n between 2 and 10 have infrasonic frequencies in the range 0.08–2 Hz. Pressure amplitudes at $r = 10 \text{ km}$ range from 10^{-4} to 50 Pa for n between 2 and 8. Only waves with $n \leq 5$ are above the typical ambient noise threshold of 10^{-2} Pa at 10 km from the weakest vortex ($V = 50 \text{ m s}^{-1}$).

Before moving on, a word of caution is in order. The reader will note that p_2 given by Eq. (5) scales as $M^{7/2}(R/r)^{1/2}$, which is a factor of $\sqrt{r/(RM)}$ greater than Lighthill’s theory would suggest. This discrepancy illus-

trates the potential danger of using two-dimensional theories to estimate the amplitude of acoustic radiation (cf. Howe 2003). Later, we will examine the effect of giving the vortex finite vertical depth.

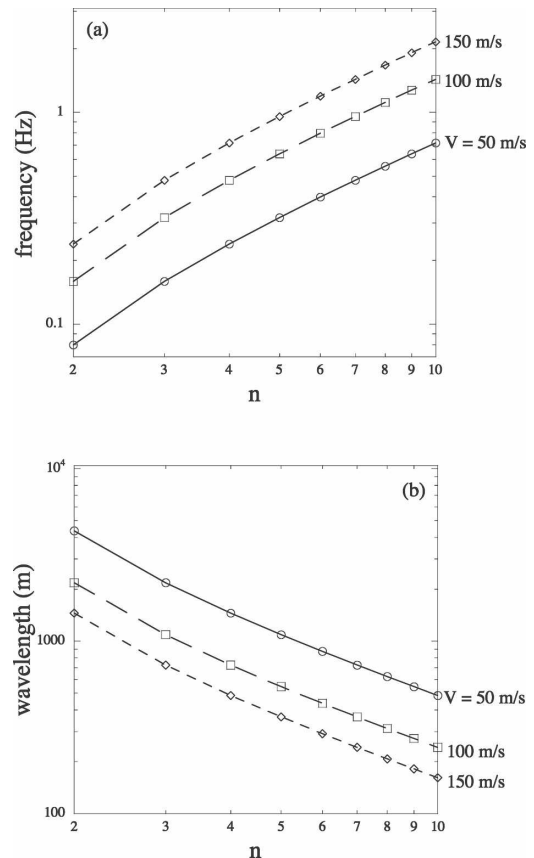


FIG. 2. (a) Frequencies and (b) radial wavelengths of the spiral acoustic waves that are generated by the discrete modes (Rossby waves) of a 2D Rankine vortex.

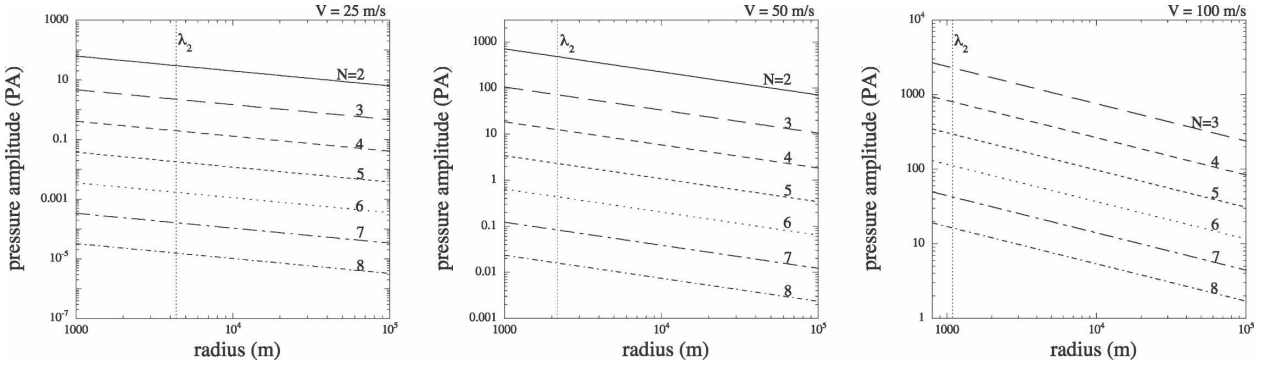


FIG. 3. Low Mach number theory [Eq. (11)] for the peak-to-peak amplitude of the dominant outward-propagating spiral acoustic wave that is generated by N corotating point vortices for (left) $V = 25$, (middle) $V = 50$, and (right) $V = 100$ m s⁻¹. As shown, the amplitude of the spiral wave decreases as 1) r increases, 2) N increases, and 3) $V = \Omega_N R$ decreases. All amplitudes are calculated with $R = 100$ m, $c_o = 347.2$ m s⁻¹, and $\rho_o = 1.16$ kg m⁻³. The dashed vertical line in each plot indicates the maximum radial wavelength (λ_2) of the spiral radiation. In principle, the plotted theory is inaccurate for $r < \lambda_2$.

c. Radiation from a 2D ring of corotating suction vortices

In theory, rings of corotating suction vortices can develop from the eyewall instability of a parent tornado at high swirl ratio (e.g., Rotunno 1978; Gall 1983). Numerous laboratory experiments and computer simulations indicate that multiple vortex states prevail when expected from stability theory (Weske and Rankin 1963; Ward 1972; Church et al. 1979; Vladimirov and Tarasov 1980; Lewellen et al. 2000; Montgomery et al. 2002), and can even emerge spontaneously from turbulence (Fine et al. 1995; Jin and Dubin 1998; Schecter et al. 1999). Moreover, there is observational evidence that multiple-vortex states can exist in real tornadoes (Wurman 2002, and references therein).

In light of these considerations, the second paradigm that we consider is acoustic radiation from a two-dimensional ring of N equally strong, equally spaced suction vortices (see Fig. 8). The vorticity distributions of such rings have the approximate form

$$\zeta(r, \varphi, t) = \sum_{j=1}^N \Gamma \frac{\delta(r - R)\delta(\varphi - 2\pi j/N - \Omega_N t)}{r}, \quad (8)$$

in which Γ is the circulation of an individual suction vortex, R is the ring radius, and δ is the Dirac distribution. The angular velocity of the ring is given by

$$\Omega_N = \frac{\Gamma(N - 1)}{4\pi R^2}, \quad (9)$$

and the Mach number by

$$M = \frac{\Omega_N R}{c_o}. \quad (10)$$

In the limit of zero Mach number, the ring is stable only if $N \leq 7$ (e.g., Havelock 1931). Although rings with $N >$

7 are theoretically unstable, they might appear temporarily in an intense tornado due to eyewall breakdown (cf. Lewellen et al. 2000).

In the radiation zone, the dominant component of the pressure perturbation satisfies the equation

$$p_N \approx \sqrt{\frac{8\pi R}{r}} \rho_o c_o^2 M^{N+3/2} \frac{N^{N+1/2}}{2^N (N-1)(N-1)!} \times \cos[N\varphi + N\Omega_N(r/c_o - t) - (2N-1)\pi/4]. \quad (11)$$

The ratio of p_N to higher-order harmonics becomes infinite with radius r . Equation (11) is derived in appendix A (cf. Howe 2003; Powell 1964).

Figure 3 shows the peak-to-peak amplitude of the radiation pressure field [Eq. (11)] as a function of radius for rings with $R = 100$ m and $\Omega_N R = 25$ m s⁻¹, 50 m s⁻¹, and 100 m s⁻¹. As before, the ambient sound speed is $c_o = 347.2$ m s⁻¹, corresponding to $p_o = 10^5$ Pa and $\rho_o = 1.16$ kg m⁻³. Figures 4a,b show the frequency and asymptotic radial wavelength of the radiation field versus the number of vortices N that compose the ring.

All rings with N between 2 and 10 have infrasonic frequencies in the range 0.08–2 Hz. Pressure amplitudes at $r = 10$ km range from 10^{-5} to 800 Pa for N between 2 and 8. For a given Mach number, the corotating suction vortices produce much stronger radiation than the Rossby waves of a vortex patch with $\epsilon = 0.1$. Nevertheless, at the lowest Mach number ($V = 25$ m s⁻¹), only rings with $N \leq 5$ produce radiation that is above the typical noise threshold of 10^{-2} Pa at 10 km.

Results for $N = 2$ and $V = 100$ m s⁻¹ were purposely removed from the plots. This system violates the estimated reality constraint

$$\frac{8MN}{\pi(N-1)} \leq 1. \quad (12)$$

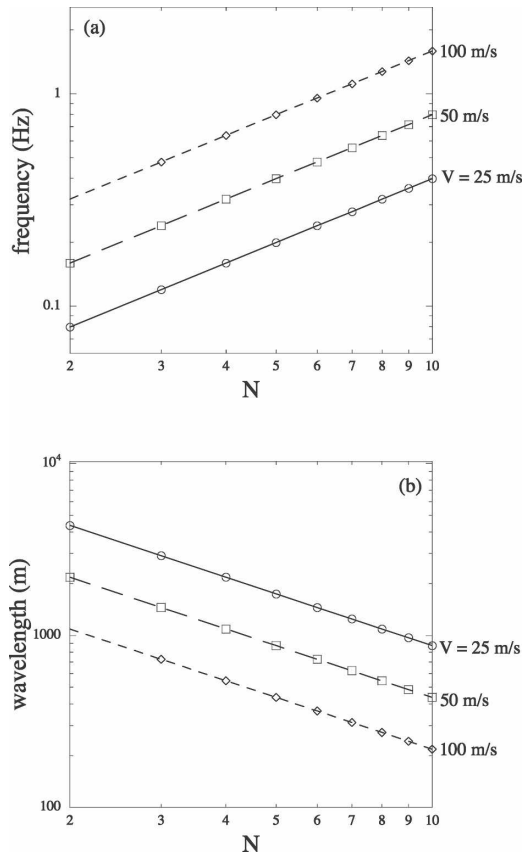


FIG. 4. (a) Frequencies and (b) radial wavelengths of the dominant spiral acoustic waves that are generated by N corotating point vortices.

Condition (12) is required for the uniform constituent vortices to have internal Mach numbers less than one-half. Here, we have assumed that the radius of a constituent vortex does not exceed $\pi R/2N$.

3. RAMS simulations of vortex sound

As explained earlier, one goal of this study is to test the adequacy of RAMS for simulating the adiabatic production of tornado infrasound. To this end, we here compare the analytical results of sections 2b and 2c to the acoustic radiation that vortices emit in RAMS. Appendix C describes the dry core of RAMS, with the modifications that were made for this study. Appendix D describes the basic procedure for initializing the vortex flow.

a. Simulated radiation from a 2D Rankine vortex

In the first set of numerical experiments, we consider a uniform columnar vortex of mean radius $R = 100$ m in a homentropic atmosphere of potential temperature

TABLE 1. Two-dimensional Rankine vortex simulations. See text (section 3a) for discussion.

Simulation	V (m s^{-1})	M	n	f_n (Hz)	λ_n (km)	$2p_n$ (Pa)
RK1	25	0.072	2	0.04	8.73	0.12
RK2	50	0.144	2	0.08	4.36	1.41
RK3	50	0.144	3	0.16	2.18	0.38
RK4	50	0.144	4	0.24	1.45	0.09
RK5	75	0.216	2	0.12	2.91	5.81
RK6	75	0.216	3	0.24	1.45	2.37
RK7	100	0.288	2	0.16	2.18	15.91
RK8	100	0.288	3	0.32	1.09	8.64
RK9	100	0.288	4	0.48	0.73	3.86
RK10	150	0.432	2	0.24	1.45	65.76
RK11	150	0.432	3	0.48	0.73	53.57

$\theta = 300$ K. The ambient atmospheric surface pressure is $p_o = 10^5$ Pa, and the ambient surface sound speed is $c_o = 347.2$ m s^{-1} . Since we are here interested in simulating 2D infrasound, the atmosphere is bounded above by a rigid wall at a mere 22 m from the surface. Accordingly, the pressure and sound speed hardly change from top to bottom.

Each simulation consists of four nested grids that are centered on the vortex. All four grids have vertical increments of 2 m. The finest grid has horizontal increments of 2 m and extends 400 m in both horizontal directions. The coarsest grid has horizontal increments of 128 m and extends 32.8 km in both horizontal directions. The lateral boundary conditions permit outward propagating acoustic radiation, as described in appendix C. In general, the simulations run for 64 s.

Table 1 displays the variables of each numerical experiment. The maximum wind speeds of the unperturbed (circular) vortices range from 25 to 150 m s^{-1} , corresponding to Mach numbers between 0.07 and 0.43. At $t = 0$ in each experiment, a sinusoidal perturbation of amplitude $\epsilon = 0.1$ is applied to the radial boundary of the vortex core. The azimuthal wavenumbers (n) vary between $n = 2$ and $n = 4$. The dominant acoustic emissions have frequencies (f_n) in the range 0.04–0.48 Hz. The corresponding radial wavelengths (λ_n) are in the range 0.73–8.73 km. The theoretical peak-to-peak radiation amplitudes ($2p_n$) at $r = 5$ km are between 0.09 and 65.76 Pa.

Figure 5a contains snapshots of the vertical vorticity distributions for several experiments. Figure 5b contains corresponding snapshots of the infrasound radiation; specifically, each plot shows the pressure perturbation minus the azimuthal mean. Note that the outer radial wavelength of the asymmetric pressure perturbation decreases [according to Eq. (7)] as either V or n increases.

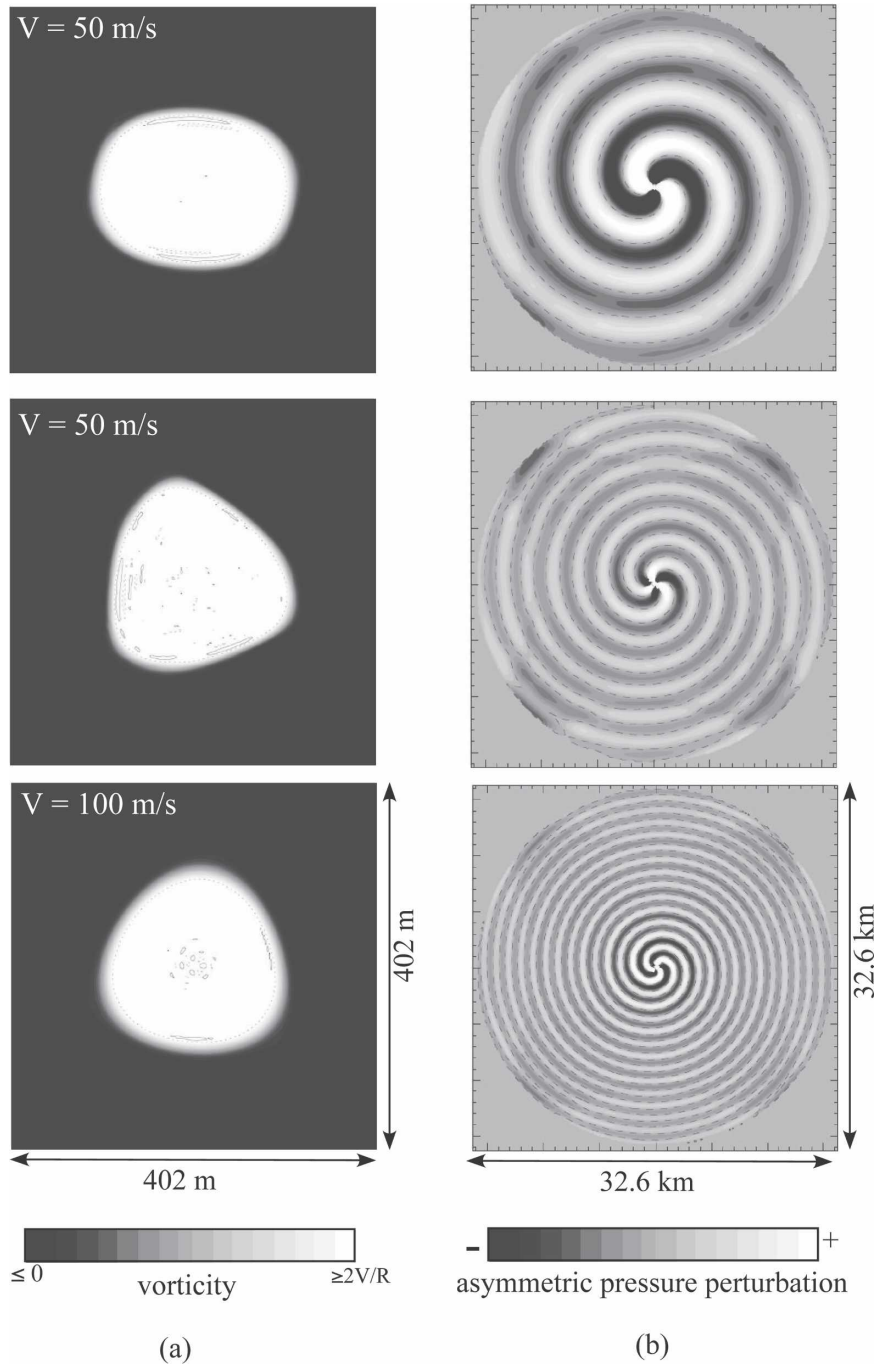


FIG. 5. Select RAMS simulations of spiral acoustic radiation from a 2D Rankine vortex. (top to bottom) RK2, RK3, and RK8. (a) Snapshots of vorticity at $t = 64$ s. (b) Snapshots of the asymmetric pressure perturbation (p minus its azimuthal mean) at $t = 64$ s.

Figure 6 plots the pressure amplitudes of the simulated radiation fields at various probe positions versus the “wave Mach number,”

$$M_{n-1} \equiv (n - 1)M. \tag{13}$$

In general, the probes were placed at radial distances $r_p = 2$ km and 5 km from the vortex center. For the weakest vortex ($V = 25 \text{ m s}^{-1}$), the 2-km probe was replaced by a 10-km probe. The probe height z_p is irrelevant for 2D experiments. The pressure amplitude

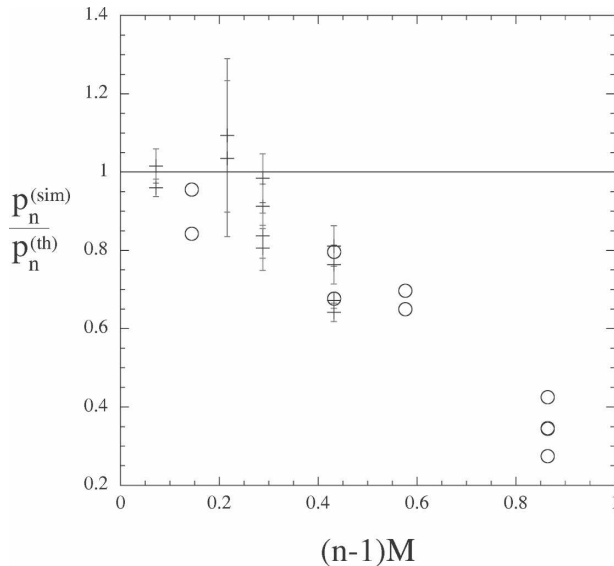


FIG. 6. Comparison of low Mach number theory [Eq. (5)] to RAMS simulations of spiral acoustic radiation from a 2D Rankine vortex. As the wave Mach number increases beyond 0.2, the simulated radiation becomes weaker than the analytical theory predicts. See text (section 3a) for details.

is here defined by the modulus of the Fourier transform

$$\hat{p}_n(t) \equiv \frac{1}{2\pi} \int_0^{2\pi} d\varphi p(r_p, \varphi, z_p, t) e^{-in\varphi}. \quad (14)$$

The plotted amplitudes are normalized to their theoretical values [one-half the coefficient of the cosine function in Eq. (5)].

The plot contains two data types. The first type (indicated by a crosshair) is an average of $|\hat{p}_n(t)|$ over tens of seconds after the radiation first reaches the probe radius r_p . First contact between the probe and the radiation field approximately occurs at time $t_* \equiv (r_p - R)/c_o$. The vertical error bars on the crosshairs indicate plus or minus one standard deviation from the mean. The second data type (indicated by a circle) is the value of an exponential fit of $|\hat{p}_n(t)|$ at $t = t_*$. This measurement was better suited for signals that slightly decayed over the course of the simulation.

To reduce the scattering of data points, we chose the wave Mach number M_{n-1} as the independent variable instead of M . This choice also has some theoretical merit. As explained in appendix A, the derivation of Eq. (5) requires that there exists a radial interval for which

$$R \ll r \ll \frac{R}{M_{n-1}}. \quad (15)$$

Therefore, the theory is increasingly inaccurate as M_{n-1} (not simply M) approaches unity. As expected, the

plotted data diverges from theory as M_{n-1} increases from zero. Moreover, the relative amplitude of the simulated radiation field decays nearly an order of magnitude as M_{n-1} increases from 0.2 to 0.86.³

To conclude, we note that the dissipation parameters were adjusted to ensure numerical convergence well within the error bars of the presented data.

b. Sensitivity to a dissipation parameter

A major concern with simulating tornado infrasound in a full thunderstorm simulation is inadequate spatial resolution or unrealistically high eddy diffusion. The eddy diffusivity is proportional to the product $C_x \Delta x \times C_z \Delta z$ [see Eq. (C8) in appendix C]. Here, Δx and Δz are the horizontal and vertical grid spacings, whereas C_x and C_z are dimensionless parameters. Multiplying both C_x and C_z by β amounts to increasing the horizontal and vertical grid spacings by the same factor.

Let us consider the effect of increasing the values of C_x and C_z on one of the above simulations. In particular, take the case in which $V = 50 \text{ m s}^{-1}$ and $n = 3$. For that experiment, C_x and C_z were set equal to 0.1. Figure 7 shows the pressure amplitude of the radiation field versus time at the 2-km probe for $\beta = 1, 2, 4,$ and 8 . For $\beta = 1$ and 2 , the amplitude is approximately constant over the course of the simulation. For $\beta = 4$, the amplitude decays to roughly one-half of its original ($t = t_*$) value. For $\beta = 8$ the amplitude decays to less than one-tenth of its original value. Decay occurs because eddy diffusion wipes out the source vortex Rossby wave.

A “high resolution” thunderstorm simulation might have a fine grid with $\Delta x = 10 \text{ m}$, $\Delta z = 50 \text{ m}$, and $C_x = C_z = 0.2$. This is comparable to setting $\beta = 22$. Evidently, it would not suffice to adequately simulate the infrasound that is generated by a low- n Rossby wave of a relatively weak tornado. More intense tornadoes would suffer even greater dissipation, since eddy diffusivity also increases with the local strain rate.

c. Simulated radiation from a 2D ring of corotating suction vortices

In the second set of numerical experiments, we consider N uniform columnar vortices that are evenly spaced along a circular ring of radius $R = 100 \text{ m}$. Each vortex is parameterized by its initial diameter d and

³ Ford (1994a) studied the analogous problem of gravity wave radiation from a shallow-water vortex. He implicitly showed that low Froude number (Mach number) theory overestimates the rate at which the radiation destabilizes the vortex, at relatively modest $Fr(M)$. This result seems consistent with Fig. 6.

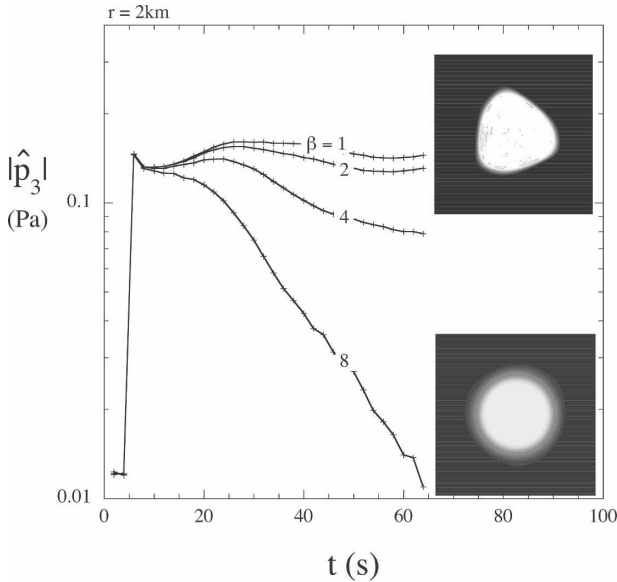


FIG. 7. Time series at $r = 2$ km of the $n = 3$ Fourier component of the radiation field of simulation RK3, with variable dissipation. As the dissipation parameter β increases toward values typical of present-day thunderstorm simulations, the radiation becomes rapidly damped. Such damping is connected to the viscous axisymmetrization of the vortex, i.e., viscosity-enhanced damping of the source Rossby wave. For $\beta = 1$ the vortex remains deformed (top inset), whereas for $\beta = 8$ the vortex is nearly circular by $t = 64$ s (bottom inset).

uniform vorticity $4\Gamma/\pi d^2$. The ambient state of the atmosphere, the boundary conditions, and the discretization parameters are the same as before (see section 3a).

Table 2 displays the variables of each numerical experiment. The vortex diameters are between $d = 50$ m and $d = 71$ m. The number of vortices N varies from 2 to 4. The maximum wind speeds of the vortices range from $V_s = 100$ m s⁻¹ to an unrealistic (but subsonic) $V_s = 283$ m s⁻¹. The Mach number of the ring [Eq. (10)] is between 0.036 and 0.192; therefore, the rotation period of the ring varies from 50.3 to 9.4 s. The dominant acoustic emissions have frequencies (f_N) in the range 0.04–0.32 Hz. The corresponding radial wavelengths (λ_N) are in the range 1.09–8.73 km. The theoretical

peak-to-peak radiation amplitudes ($2p_N$) at $r = 5$ km are between 1.71 and 318.24 Pa.

Figure 8a contains snapshots of the vertical vorticity distributions for several experiments. Figure 8b contains corresponding snapshots of the infrasound radiation; specifically, each plot shows the dominant Fourier component of the pressure perturbation. Note that the outer radial wavelength of the pressure perturbation decreases [according to Eq. (7), with $\omega_n \rightarrow N\Omega_N$] as either the Mach number M or the number of vortices N increases.

Figure 9 plots the pressure amplitudes $|\hat{p}_N|$ of the simulated radiation fields versus M . The plotted amplitudes are normalized to their theoretical values [one-half the coefficient of the cosine function in Eq. (11)]. The probe positions are at $r_p = 2$ km and/or $r_p = 5$ km. The data are represented by crosshairs or circles, depending on the procedure by which they were measured (see section 3a). As before, the simulated vortex infrasound agrees with theory at low Mach numbers, but undershoots theory as M increases toward unity.

d. Simulated radiation from a 3D vertically sheared Rankine vortex

As mentioned earlier, two-dimensional studies overestimate the amplitude of acoustic radiation from three-dimensional vortices. To illustrate this point, we here examine the radiation that is generated by an elliptically deformed Rankine vortex whose tangential winds decay exponentially with height [Eq. (D1) of appendix D] from a maximum speed of 50 m s⁻¹ at ground level. In this experiment, the ambient values of temperature (300 K) and sound speed (347.2 m s⁻¹) are constant. On the other hand, the entropy varies in both the vortex and in the environment. Although RAMS is inexact for nonhomentropic flows (appendix C), we believe that the numerical results presented here are qualitatively correct.

As before, the simulation uses four nested grids. The horizontal grid increments are 256, 64, 16, and 2 m. The corresponding grids cover 33, 6.5, 1.6, and 0.4 km in both x and y . The vertical grid has 439-m increments,

TABLE 2. Two-dimensional simulations of corotating vortices. See text (section 3c) for discussion.

Simulation	N	$\Omega_N R$ (m s ⁻¹)	M	V_s (m s ⁻¹)	d (m)	f_N (Hz)	λ_N (km)	$2p_N$ (Pa)
CV1	2	12.5	0.036	100.0	50.0	0.04	8.73	2.49
CV2	2	25.0	0.072	200.0	50.0	0.08	4.36	28.13
CV3	3	33.3	0.096	133.3	50.0	0.16	2.18	7.64
CV4	4	37.5	0.108	100.0	50.0	0.24	1.45	1.71
CV5	2	50.0	0.144	282.84	70.7	0.16	2.18	318.24
CV6	3	66.7	0.192	230.94	57.7	0.32	1.09	172.84

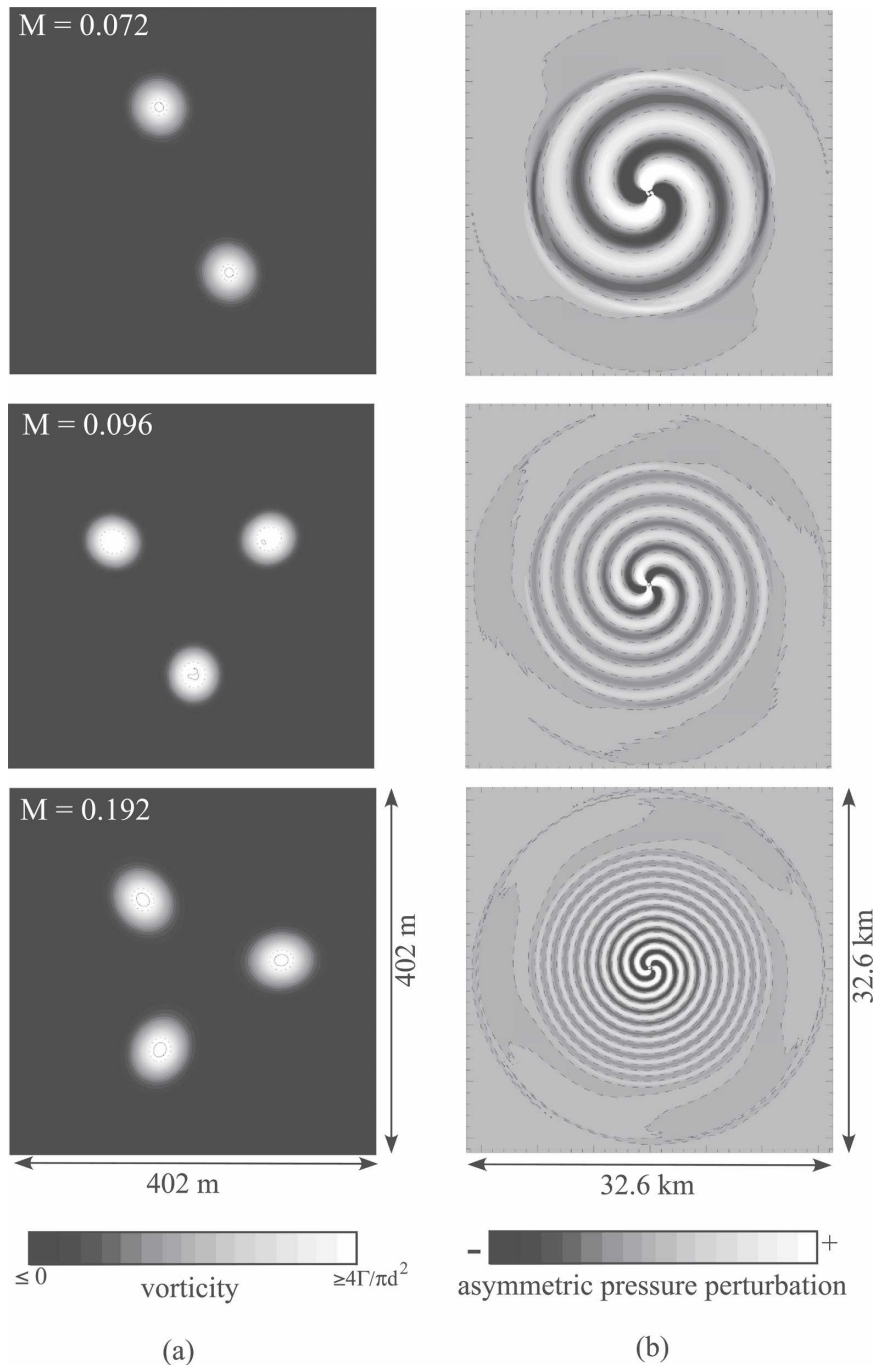


FIG. 8. Select RAMS simulations of spiral acoustic radiation from corotating vortices. (top to bottom) CV2, CV3, and CV6. (a) Snapshots of vorticity at $t = 32$ s. (b) Snapshots of the dominant component ($2\Re[\hat{p}_N e^{iN\varphi}]$) of the pressure perturbation at $t = 32$ s.

and extends to $z = 18$ km. The relatively large grid spacing in z adequately resolves the vertical variation of the vortex over the course of the simulation.

Figures 10–12 summarize the simulation. Figure 10 shows the azimuthally averaged tangential velocity, potential temperature, total pressure, and perturbation

pressure at $t = 0$ s. Figure 11 shows the state of the radiating vortex at $t = 64$ s. By this time, the elliptical ($n = 2$) perturbation has developed significant phase variation in z . Note also that the dominant radial wavelength of the infrasound increases with height.

Figure 12 illustrates various aspects of the time evo-

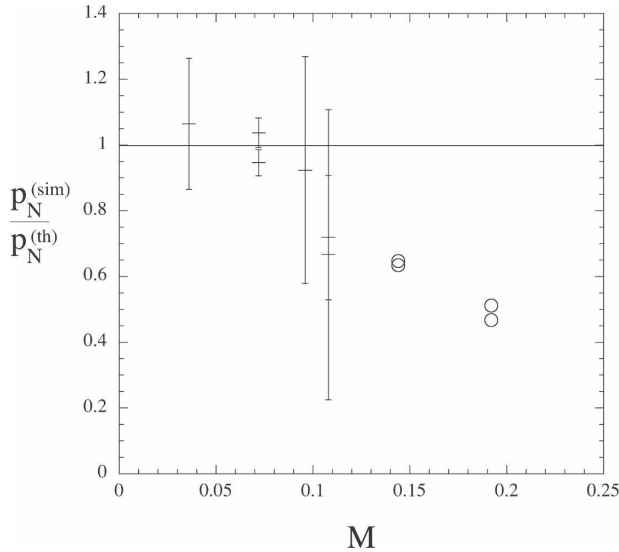


FIG. 9. Comparison of low Mach number theory [Eq. (11)] to RAMS simulations of spiral acoustic radiation from corotating vortices. As the Mach number increases beyond 0.1, the simulated radiation becomes weaker than the analytical theory predicts. See text (section 3c) for details.

lution of the pressure perturbation in the vortex and in the radiation zone. Figure 12a shows that the source vortex Rossby wave frequency is roughly constant with time and varies with height according to

$$\omega_2(z) \approx \frac{V(z)}{R}. \quad (16)$$

Here, $V(z)$ is the maximum tangential wind speed at height z , and $R = 100$ m is the radius of maximum wind. In other words, the vorticity dynamics in this experiment is approximately layer-wise two-dimensional [cf. Eq. (4)]. Of course, the radiation field is a superposition of the infrasound that is generated by the vortex at each vertical level. Unlike the core Rossby waves, its frequency is substantially nonmonochromatic at fixed z (Fig. 12b).

Figure 12c shows the amplitude of the infrasound near the surface at $r = 2$ km and at $r = 5$ km. At 2 km, the amplitude decays from 74% to 21% of the infrasound that would arise from a 2D homentropic vortex patch with $V = 50 \text{ m s}^{-1}$, $c_o = 347.2 \text{ m s}^{-1}$, $p_o = 10^5 \text{ Pa}$, and $\epsilon = 0.1$. At 5 km, the amplitude decays from 41% to 13% of 2D theory. Greater attenuation at 5 km is consistent with 3D spreading of acoustic power.

For future consideration (section 5), we ran another simulation with $V(0) = 100 \text{ m s}^{-1}$. In this case, the balanced vortex had slightly negative static stability near the surface. The resulting slow gravitational instability appeared to have little influence on the $n = 2$ spiral

radiation over the short time interval considered here. The amplitude of the $n = 2$ radiation field is later discussed in connection to Fig. 18.

4. RAMS simulation of a nontornadic thunderstorm

Having verified that with sufficient resolution RAMS can adequately simulate tornado infrasound (see Figs. 6 and 9), we now turn our attention to the 0.1–10-Hz acoustic radiation that is produced in a RAMS simulation of a nontornadic thunderstorm. Nicholls and Pielke (1994a,b, 2000) previously used RAMS to simulate the emission of low-frequency (order 10^{-3} Hz) compression waves from a convective storm. Nevertheless, the following case study is the first of its kind that begins to resolve the production of infrasound from diabatic turbulence in the heart of the storm. Although we have not performed the multitude of sensitivity tests that are required for definitive results, we believe that the following discussion has value for guiding subsequent numerical research. Future tests should include changing the moisture parameterization scheme and increasing the spatiotemporal resolution beyond our current practical limits.

Before moving on, we note one obvious shortcoming of current mesoscale models, such as RAMS, for the present study: simulated thunderstorms have no thunder. Few (1969) and Few et al. (1967) reviewed observations and theory showing that the dominant acoustic energy of thunder falls in the low audio. This is consistent with the work of Georges (1976) who found no theoretical or observational evidence for a correlation of electromagnetic sources and infrasound. More recently, we have found correlations between infrasound and sprite activity (Bedard et al. 1999), but the short, impulsive nature of the signals were quite different from those related to tornadic storms.

a. Model configuration and initialization

As in the vortex experiments, the thunderstorm simulation uses a fully compressible dry core. The reader may consult appendix C for a brief description. Unlike the vortex experiments, the model is now complicated by moisture. Moisture can take the form of vapor, cloud droplets, rain, pristine ice, snow, aggregates, graupel, and hail (Walko et al. 1995). Details of the moisture parameterization are the same as in Nicholls and Pielke (2000); notably, it employs a single moment scheme.

As in the vortex simulations, the thunderstorm simulation has four nested grids. The outer (coarse) grid provides ample coverage of the storm environment.

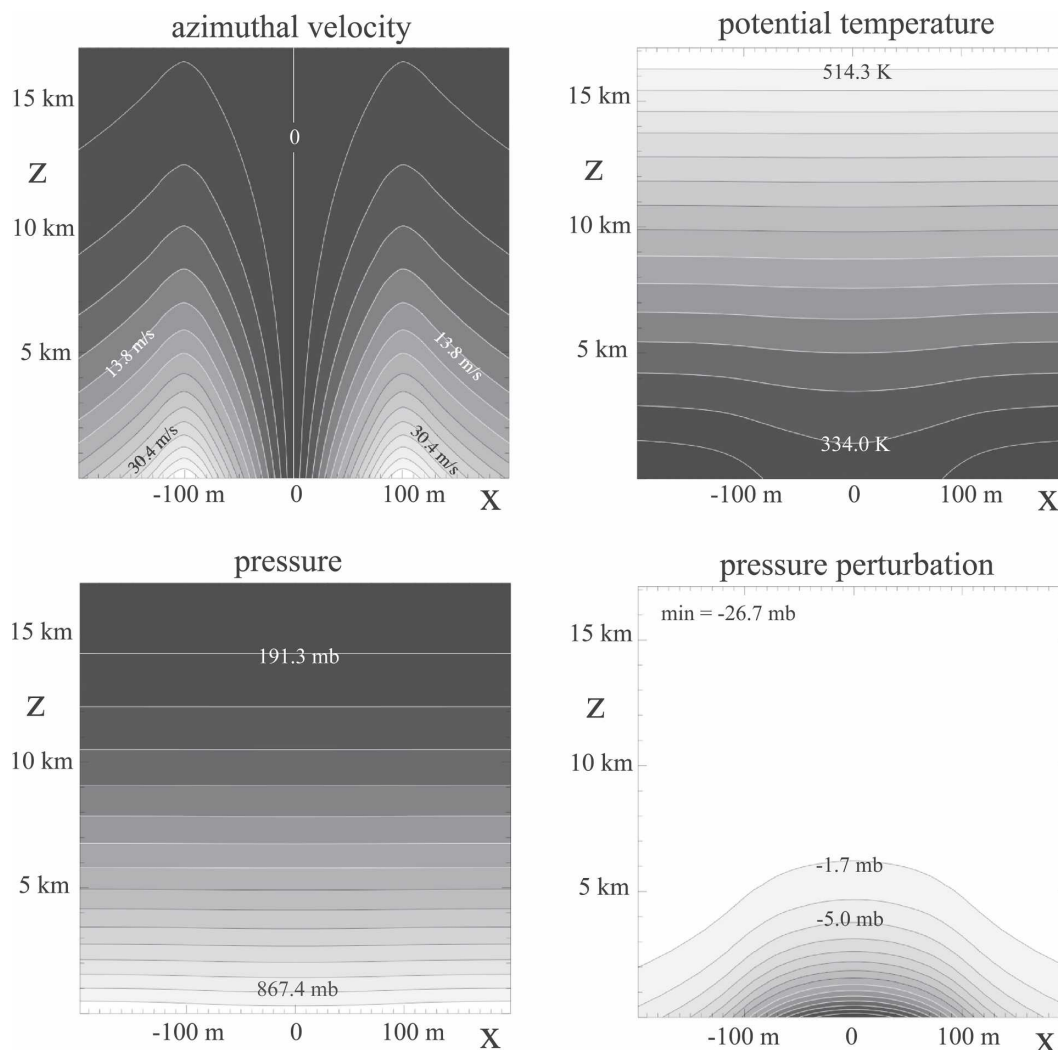


FIG. 10. The azimuthally averaged fields of a 3D elliptically deformed Rankine vortex at $t = 0$. The pressure perturbation is here defined as p minus $p_o(z)$. All contours in a given plot are evenly spaced.

The inner (fine) grid marginally resolves 100-m-scale diabatic turbulence in the most active central region of the storm. The horizontal grid increments are 1080, 270, 90, and 30 m. The corresponding grids cover 140, 28, 12, and 6 km in both x and y . The vertical grid increment is 5 m at the surface and is stretched over 200 points to 463 m at the top of the domain ($z = 20.2$ km).

At the horizontal boundaries of the outer grid, we apply Klemp–Wilhelmson (1978) radiation conditions with $c_* = 330 \text{ m s}^{-1}$. This value of c_* lets outward propagating acoustic waves leave the simulation domain. The reflection of slower-moving gravity waves is of little concern over the short time scale of the simulation, since the outer boundary is sufficiently far from the convective storm. The top boundary is buffered by an 8-km-deep dissipative layer that reduces the reflec-

tion of upward propagating disturbances. The bottom boundary is a flat rigid wall. Surface fluxes of heat, moisture, and momentum are turned off.

Figure 13 shows the vertical variation of the ambient temperature and dewpoint temperature of the simulation. Both profiles are based on the 17 July 1973 soundings of the Florida Area Cumulus Experiment. Similar profiles were used by Nicholls et al. (1991) in their numerical studies of gravity wave emission by convective storms. Here, the boundary layer is a bit closer to adiabatic in order to better represent late-day conditions, after surface warming has occurred. The initial condition of the simulation has no ambient wind. The convective storm was triggered by 30 s of low-level heating in the center of the finest grid, which produced a warm bubble.

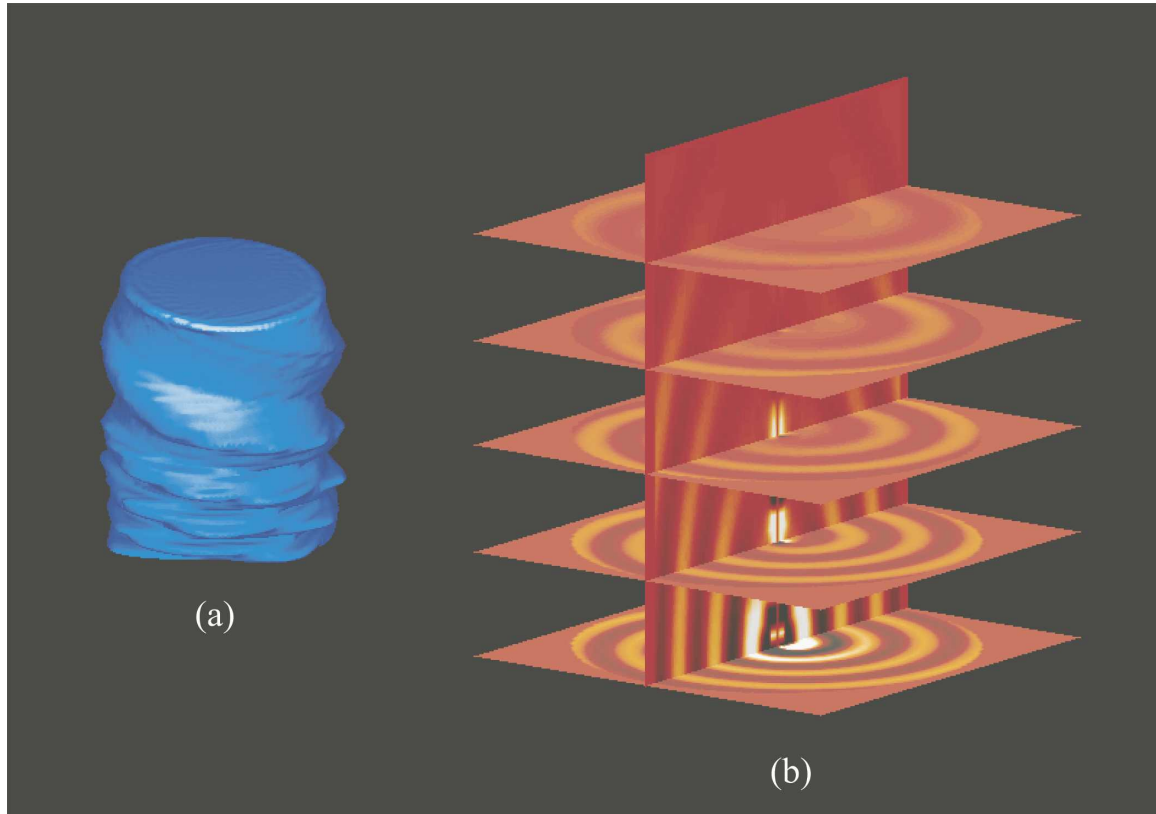


FIG. 11. Radiating “tornado” at $t = 64$ s. (a) Isosurface of $\zeta e^{z/h_v}$, in which ζ is vertical vorticity and $h_v = 6$ km is the scale height of the vortex. The isosurface corresponds to 0.3 s^{-1} , and roughly outlines the elliptical vortex core (with mean radius $R = 100$ m). Over time, the phase of the elliptical deformation develops notable variation with height, as shown here. (b) The dominant $n = 2$ component of the pressure perturbation at $t = 64$ s. Bright and dark shades represent positive and negative anomalies, respectively. The horizontal slices are $32.5 \text{ km} \times 32.5 \text{ km}$, and are at $z = 220 \text{ m}$, 3.7 km , 7.2 km , 10.8 km , and 14.3 km . The vertical slice is cut through the middle of the vortex.

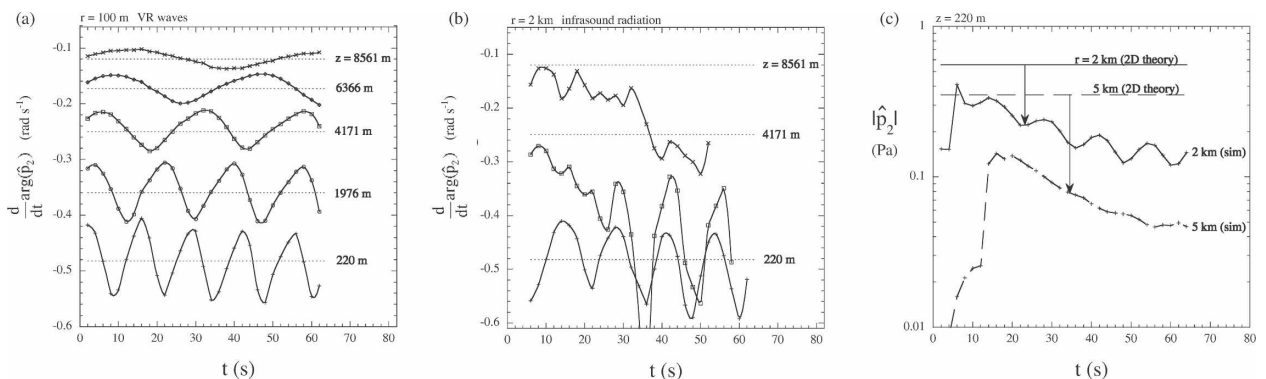


FIG. 12. Select probe measurements of the pressure perturbation inside and outside of the 3D “tornado.” (a) Time series of the oscillation frequency of the $n = 2$ component of the pressure perturbation at $r = 100$ m for several values of z . The dashed lines are local 2D Rossby wave frequencies [Eq. (16)]. Evidently, this perturbation acts like a stack of vertically decoupled Rossby waves over the time period under consideration. (b) Time series of the oscillation frequency of the $n = 2$ component of the pressure perturbation at $r = 2$ km for several values of z . Presumably, the upward propagation of strong high-frequency infrasound accounts for the observed frequency acceleration at high altitudes. (c) Time series of the amplitude of the $n = 2$ component of the pressure perturbation at $z = 220$ m for two values of r in the radiation zone. The dashed lines indicate the theoretical amplitudes of the radiation field that is created by the $n = 2$, $\epsilon = 0.1$ Rossby wave of a 2D Rankine vortex with $V = 50 \text{ m s}^{-1}$ and $R = 100$ m.

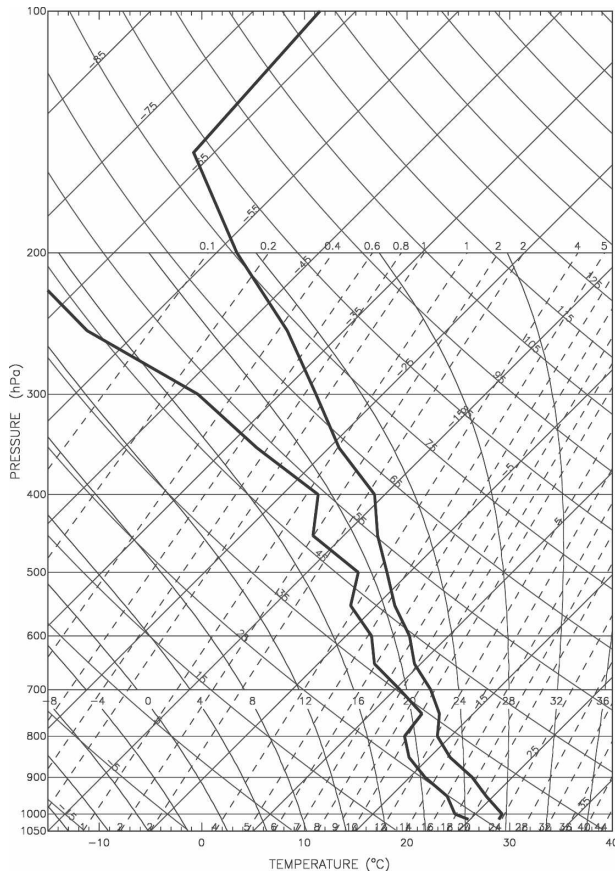


FIG. 13. Ambient temperature (thick right curve) and dewpoint temperature (thick left curve) of the thunderstorm simulation, on a traditional skew T -log p graph.

b. Brief description of the nontornadoic thunderstorm

The warm bubble quickly formed an updraft. By 20 min, the updraft developed into a towering cumulonimbus. At this stage, the cloud was composed mainly of liquid water, reached 7 km high, and spanned 2–3 km parallel to the ground. Between 25 and 30 min, the maximum value of the main updraft speed was between 30 and 35 m s^{-1} . By 30 min, the cloud top reached 14 km. Moreover, a low-level downdraft formed at the edge of the cloud, creating a weak surface outflow.

As the downdraft and surface outflow intensified, the storm developed considerable asymmetry. Figure 14 illustrates the turbulent flow structure at 34 min 19 s. The strongest updrafts and downdrafts are about 30 m s^{-1} in the upper and middle troposphere, respectively. The horizontal velocities reach about 20 m s^{-1} in various locations. Figure 15 shows a vertical cross section of the cloud structure through the center of the storm. The combined liquid and ice mixing ratio r_{il} displays a spreading anvil in the upper troposphere. The value of

r_{il} is relatively large near the melting level, between $z = 3$ and 5 km.

c. The acoustic radiation field

Figure 16 illustrates the acoustic radiation of the thunderstorm during a small fraction of the 34th minute of the simulation. The contour plots are of the difference (p'_d) between the local pressure perturbation and its sliding average over a 10-s window: $p'_d \equiv p' - \langle p' \rangle$, in which $\langle p' \rangle = (1/10s) \int_{t-5s}^{t+5s} p' dt$. Loosely speaking, p'_d accounts for all waves that have frequencies at or above 0.1 Hz, and wavelengths at or below a few kilometers. These waves appear to emanate from the vicinity of the melting level, where diabatic processes involving hail are active (suggesting that microphysics might be an important issue for refining future simulations of thunderstorm noise). In addition, the lowest frequency component of p'_d dominates.

Figure 17a shows the power spectra of acoustic radiation at several locations. All probes were positioned at 2 m above the ground, but their horizontal distances from the storm center varied from 3.4 to 10.9 km, as indicated. All three spectra have roughly the same form, but the peak amplitude decays with increasing radius, as expected. The steep descent of each power spectrum beyond 0.1 Hz is reminiscent of the $f^{-7/2}$ decay that is expected at high frequencies for the radiation of ideal homentropic turbulence (Meecham and Ford 1958). However, direct comparison to such a theory seems unwarranted, given the diabatic nature of the source region.

The parameters that were used to compute each power spectrum are summarized in Table 3. At each probe, we performed a least squares fourth-order polynomial curve fit of the pressure perturbation p' in the variable $t' \equiv t - t_o$ over the interval $0 \leq t' \leq t_f - t_o$. We then defined the residual pressure anomaly $p'_{\text{res}} \equiv p' - p'_{\text{fit}}$. Each displayed power spectrum of p'_{res} is the product of a popular numerical recipe (SPCTRM; Press et al. 1992). Essentially, the algorithm averages k periodograms of overlapping segments of $2m$ data points that are evenly separated by the time increment dt . A Bartlett window is applied to each segment prior to computing its periodogram. The output power spectrum is discretized in frequency space with a grid increment of $df = 1/(2mdt)$. Here, each power spectrum is normalized so that the sum of its components times df approximately equals the mean square amplitude of p'_{res} . The zero frequency values of the power spectra are not shown, but are less than the values at df .

Note that the very low amplitude pressure fluctuations at the highest frequencies are unphysical. Above an acoustic cutoff, $f_{\text{ac}} \equiv c_o/(4\Delta x)$, the simulation does

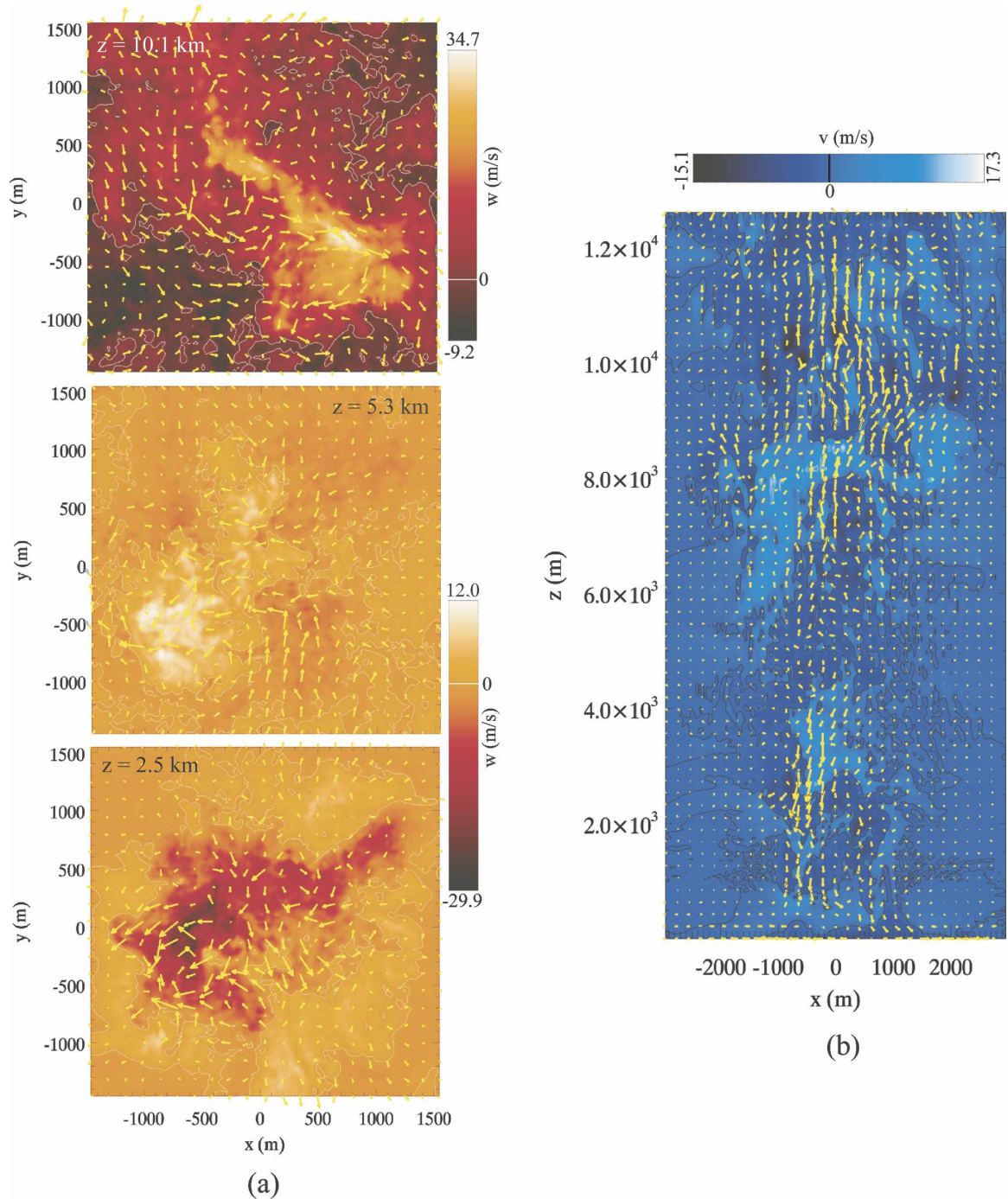


FIG. 14. Velocity fields of the simulated nontornadic thunderstorm at $t = 34 \text{ min } 19 \text{ s}$. (a) Horizontal velocity vectors superposed on contour plots of the vertical velocity (w) at $z = 2.5 \text{ km}$, $z = 5.3 \text{ km}$, and $z = 10.1 \text{ km}$. The largest velocity vectors of the top and bottom two graphs have magnitudes of 19.5 and 10.6 m s^{-1} , respectively. (b) The u - w velocity vectors superposed on a contour plot of the u velocity v at $y = 0$. The largest velocity vector has a magnitude of 30.2 m s^{-1} .

not resolve sound waves. The three probes considered here lie on separate grids with different values of f_{ac} . Table 3 lists these values, using the ground level sound speed $c_o = 347.6 \text{ m s}^{-1}$ and Δx in the range of 30–270 m.

We have also examined the power spectra of the pressure signals after basic linear detrending. The results are almost indistinguishable from those in Fig. 17a, for frequencies greater than df .

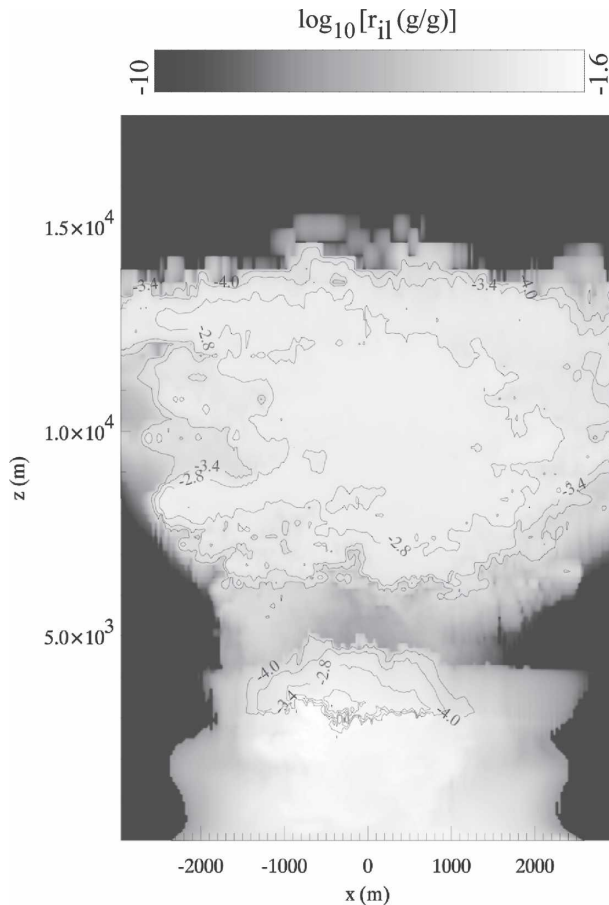


FIG. 15. Logarithmic contour plots of the liquid-ice mixing ratio (shading) and the ice mixing ratio (solid curves) in the simulated thunderstorm at $t = 34$ min 19 s and $y = 0$.

Figure 17b shows filtered (dashed) and unfiltered (solid) time series for the residual pressure perturbation at each probe. Table 4 lists the filtering parameters. A discrete Fourier transform was performed on p'_{res} between times t_o and t_f . The frequency spacing of the transform is given by df . The filtered data are the inverse of the Fourier transform, neglecting all components with frequencies less than f_1 or greater than f_2 . In each case, the value of f_1 is approximately 0.1 Hz. The value of f_2 is the minimum of the Nyquist frequency f_{max} or 10 Hz. The 0.1–10-Hz passband covers most of the structure of the simulated thunderstorm signal during the period of measurement.

5. Comparison of thunderstorm and “tornado” infrasound

If a generic thunderstorm in a shear-free environment produces stronger infrasound than a tornado,

then there would be little hope that tornado infrasound is distinguishable from the background noise of a supercell. However, our numerical simulations suggest that acoustic radiation from a generic thunderstorm is relatively weak.

Figure 18a plots the amplitude of the ground-level ($z = 2$ m) infrasound of the simulated nontornadic thunderstorm of section 4 versus distance from the middle of the storm. Each solid square is centered at the average peak-to-peak amplitude of the filtered and unfiltered pressure signals that appear in Fig. 17b. The vertical span of each square exceeds the difference between the two data types. From Table 4, the passbands of the filtered data are 0.1–10 Hz at $r = 3.4$ km, 0.1–5 Hz at $r = 5.1$ km, and 0.1–2.5 Hz at $r = 10.9$ km. The empty squares are the same measurements from a similar thunderstorm simulation in which the finest horizontal grid spacing is 90 m. Notably, this lower resolution seems to cause stronger infrasound. Given the decay of simulated infrasound with Δx , we are encouraged to interpret the simulation data as an upper bound on the level of acoustic radiation from disorganized moist convection that is several kilometers wide. Important studies of infrasound sensitivity to the grid resolution, the subgrid-scale turbulence parameterization, and the microphysics parameterization are beyond the scope of this seminal discussion, and are deferred to a future time.

Figure 18a also plots the low-level ($z = 220$ m) spiral infrasound that radiates from the three-dimensional elliptical “tornado” of section 3d. Unlike the simulated thunderstorm, the simulated tornado has an isothermal environment ($T = 300$ K). We do not expect this minor discrepancy to substantially affect our conclusions.⁴ The empty and solid circles represent radiation from the tornado at maximum wind speeds of $V = 50$ m s⁻¹ and $V = 100$ m s⁻¹, respectively. The 50 m s⁻¹ vortex produces 0.1-Hz radiation, whereas the 100 m s⁻¹ vortex produces 0.2-Hz radiation. The infrasound of the 50 m s⁻¹ vortex has the same order of magnitude as the simulated thunderstorm signal. On the other hand, the 100 m s⁻¹ vortex has a much larger signal that is quite distinct. Note that the infrasound of multiple corotating vortices can greatly exceed the infrasound of an elliptical vortex, according to section 2, and can therefore also exceed the thunderstorm noise.

For reference, the dotted lines in Fig. 18a represent estimated acoustic signals from patches of 3D homon-

⁴ Here, we are analyzing infrasound at relatively close distances from the source. Beyond roughly 20 km, atmospheric refraction can greatly influence low-level signals (Jones et al. 2004).

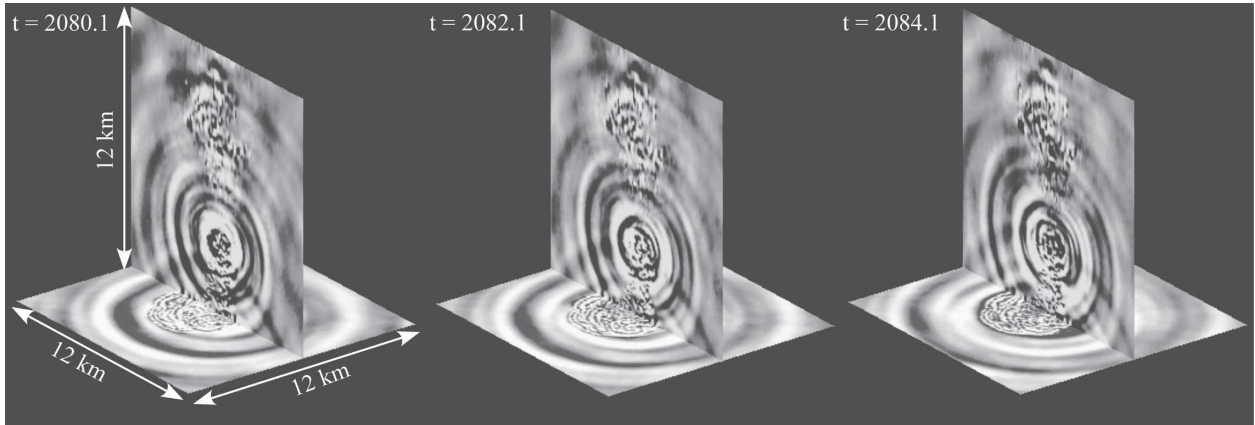


FIG. 16. Select snapshots of the 0.1-Hz (and faster) infrasound that radiates from the simulated thunderstorm. The horizontal slices are at $z = 2$ m, and the vertical slices cut through the center of the storm. The contour shading ranges from -0.126 Pa (black) to $+0.126$ Pa (white). Striking spherical waves are seen to propagate outward from a compact region in the neighborhood of the melting level. Time t is measured in seconds from the initialization of the convective updraft.

tropic vortical “turbulence” [twice the right-hand side of Eq. (1), with $c_o = 347.2 \text{ m s}^{-1}$ and $\rho_o = 1.16 \text{ kg m}^{-3}$]. The top line (LH₁₀₀) corresponds to turbulence with characteristic velocity $V = 100 \text{ m s}^{-1}$ and length scale $L = 100$ m. The bottom line (LH₂₅) corresponds to turbulence with $V = 25 \text{ m s}^{-1}$ and $L = 25$ m. In both cases, the characteristic frequency ($V/2\pi L$) is 0.16 Hz. LH₁₀₀ might be similar to the infrasound that is produced by a tornado of great intensity, whereas LH₂₅ might better correspond to a weak tornado. Clearly, LH₁₀₀ is much stronger than the acoustic signal of an ordinary simulated thunderstorm (squares), whereas LH₂₅ is much weaker.

Figure 19 more directly addresses the potential importance of infrasound that is adiabatically generated by 3D vortical turbulence, that is, Lighthill radiation. We here speculate that Lighthill radiation is important if

- (i) the characteristic frequency of the turbulence is in the 0.1–10-Hz frequency band, and
- (ii) the Mach number of the turbulence is sufficiently high for the amplitude of the radiation pressure field to equal or exceed an estimated nonsevere weather value of, say, 0.25 Pa at $|\mathbf{x}| = 5$ km [see Fig. 18a (squares)].

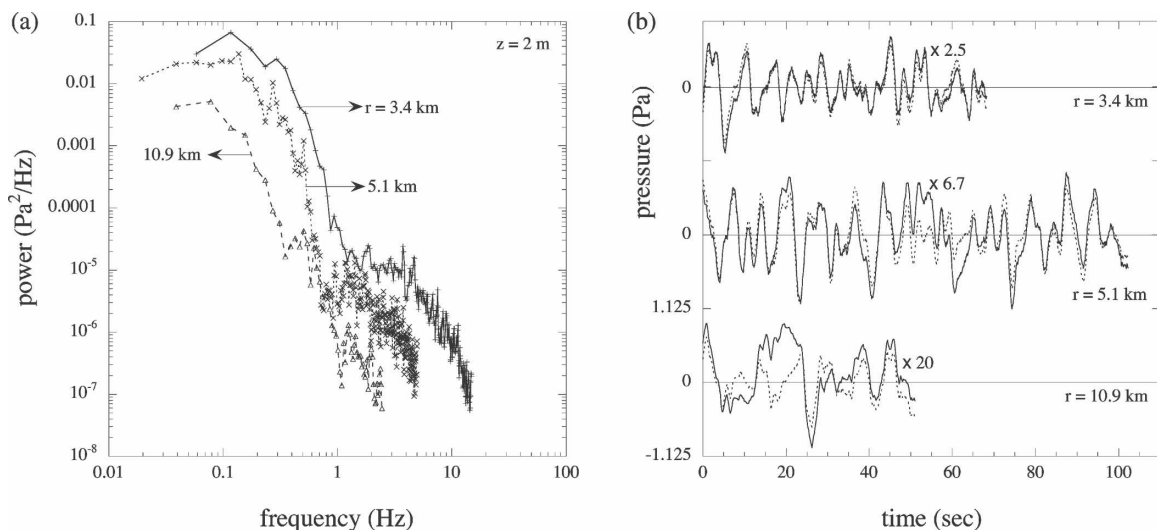


FIG. 17. Probe measurements of the infrasound from the simulated thunderstorm. (a) Power spectra of the residual ground-level (2 m) pressure perturbation at several radii. (b) Filtered (dashed) and unfiltered (solid) time series of the residual pressure perturbation at the same locations. The top, center, and bottom curves are magnified by factors of 2.5, 6.7 and 20, respectively.

TABLE 3. Power spectra parameters. See text (section 4c) for discussion.

Probe radius (km)	t_o (s)	t_f (s)	dt (s)	df (Hz)	f_{max} (Hz)	m	k	f_{ac} (Hz)
3.4	2000.0	2110.9	0.033	0.059	15.0	256	6	2.9
5.1	1999.8	2127.7	0.10	0.020	5.0	256	2	1.0
10.9	2064.0	2127.8	0.20	0.039	2.5	64	2	0.3

TABLE 4. Filtered time series parameters. See text (section 4c) for discussion.

Probe radius (km)	t_o (s)	t_f (s)	df (Hz)	f_1 (Hz)	f_2 (Hz)
3.4	2000.0	2068.3	0.007	0.09	9.99
5.1	1999.8	2102.1	0.005	0.10	5.00
10.9	2064.0	2115.0	0.010	0.10	2.5

Figure 19 shows the region in V - L parameter space where both conditions (i) and (ii) are satisfied. To construct this diagram, the amplitudes of p' were estimated by the right-hand side of Eq. (1). Note that the ampli-

tude of the infrasound (at 5 km) can exceed the estimated 0.25-Pa threshold only if the characteristic velocity of the turbulence (V) is greater than about 40 m s^{-1} , and if the characteristic length scale is less than

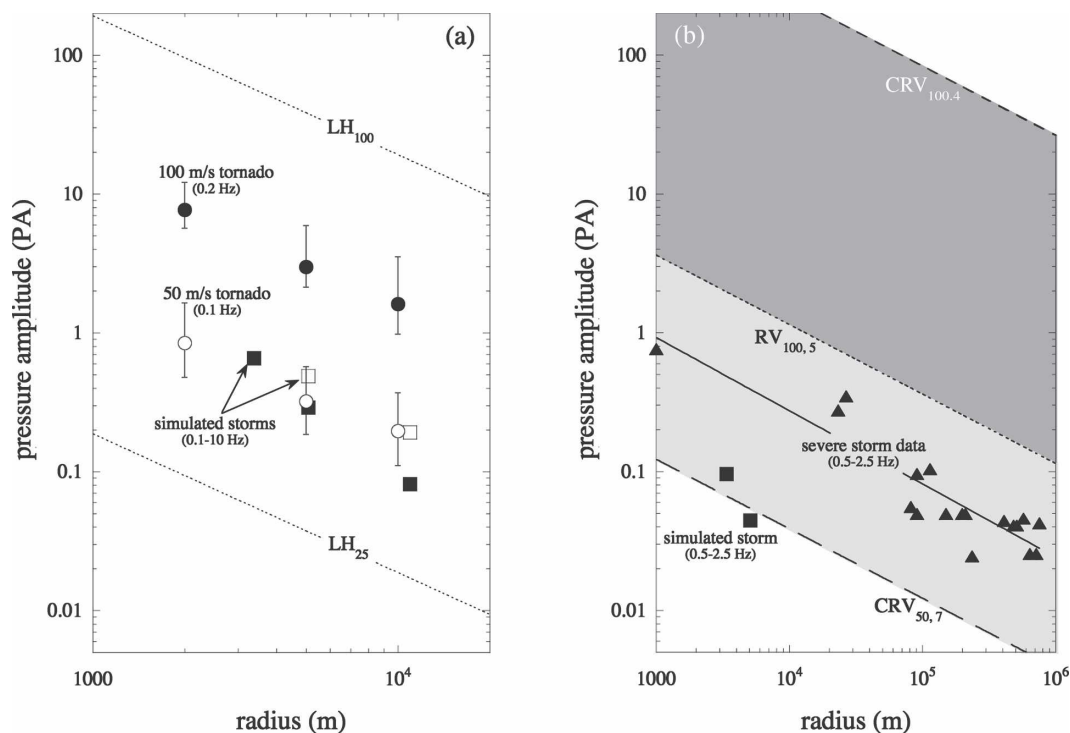


FIG. 18. Comparison of tornado infrasound and thunderstorm noise. (a) Select RAMS simulations. The circles represent spiral radiation (of order 0.1 Hz) from 3D vertically sheared Rankine vortices with 50 m s^{-1} (empty) and 100 m s^{-1} (solid) maximum tangential wind speeds. The squares represent the 0.1–10-Hz radiation from a simulated nontornadoic thunderstorm in which the finest horizontal grid spacing is either 30 m (filled) or 90 m (empty). For reference, the dotted lines are Lighthill's estimates of the acoustic radiation from 3D homentropic "turbulence," with a characteristic frequency of 0.16 Hz and a characteristic velocity of either 25 m s^{-1} (LH₂₅) or 100 m s^{-1} (LH₁₀₀). (b) Observed infrasound. The triangles (fitted with a solid line) represent the observed 0.5–2.5-Hz infrasound that radiates from severe weather systems (Bedard 2005). For reference, the squares represent the 0.5–2.5-Hz radiation from the simulated nontornadoic thunderstorm, in which the finest horizontal grid spacing is 30 m. For additional reference, each broken line represents the maximum level of spiral radiation, faster than 0.5 Hz, that a specific 2D tornado-like flow can produce. The top (CRV_{100,4}) and bottom (CRV_{50,7}) lines correspond to rings of corotating vortices with $V = 100 \text{ m s}^{-1}$ and $V = 50 \text{ m s}^{-1}$, respectively. In both cases, the ring radius is 100 m. At $V = 100 \text{ m s}^{-1}$, the ring can produce fast radiation only if $N \geq 4$; the radiation amplitude descends from the dark gray to the white region of the graph with increasing N . At $V = 50 \text{ m s}^{-1}$, the ring can produce fast radiation only if $N \geq 7$, and only in the white region of the graph. The middle line (RV_{100,5}) corresponds to a deformed Rankine vortex with $V = 100 \text{ m s}^{-1}$, $R = 100 \text{ m}$, and $\epsilon = 0.1$. The Rossby waves of this vortex (with $n \geq 5$) can produce spiral acoustic waves faster than 0.5 Hz in the light gray or white regions of the graph.

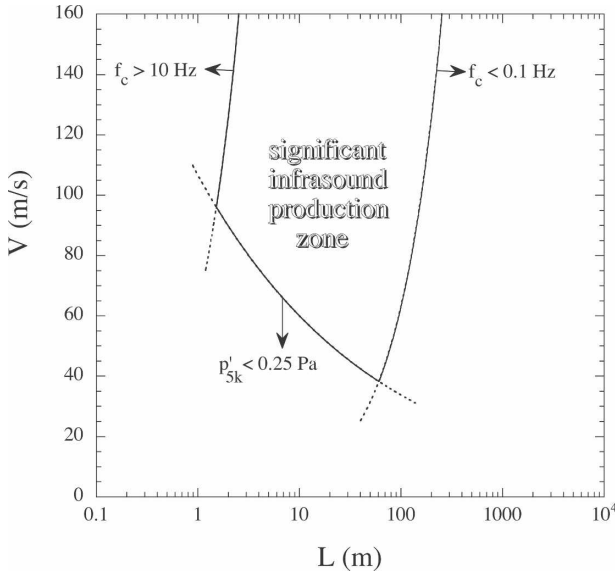


FIG. 19. Estimated region of parameter space in which compact vortical “turbulence” can adiabatically produce 0.1–10-Hz infrasound above that measured from the simulated nonsevere thunderstorm. The turbulent flow has characteristic velocity V and length scale L . Its characteristic frequency is $f_c = V/(2\pi L)$. The turbulence produces acoustic radiation with pressure anomaly p' . To equal or exceed the simulated thunderstorm signal, p' should equal or exceed roughly 0.25 Pa at 5 km from the center of the storm.

a few hundred meters. Although much higher velocity flows at smaller scales would produce notable signals, their existence would be extraordinary in any terrestrial storm system.

Let us now briefly turn our attention to field measurements. Acoustic radiation from severe thunderstorms was analyzed most recently by Bedard (2005). In his study, almost all of the thunderstorms that generated significant infrasound (between 0.5 and 2.5 Hz) were observed to have hail, radar hook echoes, or cloud tops greater than 45 000 ft. Figure 18b (triangles) shows the pressure amplitude of the 0.5–2.5-Hz infrasound versus distance from various storms. Between 1 and 10³ km, the amplitude decays roughly as $r^{-1/2}$ (solid line) from order 1 Pa to order 0.01 Pa. Nongeometric decay might be an artifact of different source strengths, or indicate vertical trapping of acoustic energy by ambient wind shear and thermal stratification. In principle, the excitation of surface waves could also produce nongeometric decay (Piercy et al. 1977; Tolstoy 1984; Howe 1985; Daigle et al. 1996); however, we know of no complementary evidence that clearly proves the existence of atmospheric surface waves that propagate over long distances in the frequency band of interest. On the other hand, ray trace simulations that predict vertical

trapping by wind and temperature gradients can also predict observed shadow zones, or regions in which the signal energy is effectively zero (Jones et al. 2004).

The field measurements of acoustic radiation from severe weather are almost entirely beyond 20 km, where 0.5–2.5-Hz acoustic waves are not adequately resolved by the thunderstorm simulation. Nevertheless, we have plotted the 0.5–2.5-Hz infrasound signal of the simulated thunderstorm (squares) at 3.4 and 5.1 km, where it is marginally credible. The trend of observational data (the solid line) suggests that severe weather signals would be an order of magnitude higher than the simulated thunderstorm signal in this region. Accordingly, we speculate that a larger or more violent storm, perhaps one that includes a tornado, would be necessary to reproduce the observed 0.5–2.5-Hz infrasound.

Because the field data suggest vertical trapping of acoustic energy, there is some rationale for comparing them to the theoretical infrasound of the 2D “tornado” of section 2. The short-dashed line at the top of Fig. 18b (CRV_{100,4}) marks the maximum peak-to-peak pressure amplitude of fast (>0.5 Hz) radiation from a ring of N corotating point vortices, with $V = 100 \text{ m s}^{-1}$ and $R = 100 \text{ m}$. Specifically, it corresponds to the 0.64-Hz spiral wave that is produced when $N = 4$. The long-dashed line (CRV_{50,7}) marks the upper bound of fast radiation from a similar ring of N corotating point vortices, but with $V = 50 \text{ m s}^{-1}$. Specifically, it corresponds to the 0.56-Hz spiral wave that is produced when $N = 7$. The short-dashed line (RV_{100,5}) marks the upper bound of fast radiation from a deformed Rankine vortex with $V = 100 \text{ m s}^{-1}$, $R = 100 \text{ m}$, and $\epsilon = 0.1$. It corresponds to the 0.64-Hz infrasound of the $n = 5$ vortex Rossby wave. The 2D theory curves considered here are best viewed as generous upper extremes on the radiation levels from genuine 3D tornadoes of similar form. At the 2D extreme, both of the 100 m s^{-1} tornadoes considered here could account for the observed high-frequency infrasound (triangles) from severe weather systems, whereas the 50 m s^{-1} tornado could not. Note that all of the theory curves were obtained from Eqs. (5) and (11), with $c_o = 347.2 \text{ m s}^{-1}$ and $\rho_o = 1.16 \text{ kg m}^{-3}$.

6. Suppression of spiral radiation by critical layers

Above, we showed that the Rossby-like waves of a sufficiently intense tornado can generate 0.1–10 Hz infrasound that exceeds the noise of a simulated nontornadoic thunderstorm. We have already addressed the possible suppression of vortex Rossby waves by eddy viscosity. For completeness, we must also address inviscid damping mechanisms.

To this end, we first note that the theory of tornado infrasound is analogous to the theory of gravity wave radiation from mesoscale atmospheric vortices, such as hurricanes and supercell mesocyclones (Ford 1994a,b; Polvani et al. 1994; Chimonas and Hauser 1997; Plougonven and Zeitlin 2002; Chow and Chan 2003). Schecter and Montgomery (2004, 2006, 2007) recently showed that critical layers can effectively damp the Rossby waves of inviscid mesoscale cyclones, and thereby inhibit their production of gravity waves. The following relates the shallow-water analysis of Schecter and Montgomery (2006) to the problem of acoustic radiation from a 2D homentropic vortex.

a. Perturbation equations

It is not our intention to present lengthy derivations. Nevertheless, it is important to state the equations that form the basis of the presented theory. We will start with the equations for small perturbations about an axisymmetric vortex. We will write these equations in a general form that applies to both the shallow-water model and the 2D homentropic gas model, so that the connection between gravity wave and acoustic radiation is clear. We will use a notation in which overbars and primes indicate equilibrium and perturbation fields, respectively, and no dressing indicates the sum of the two.

To begin with, the equilibrium vortex is characterized by its azimuthal velocity field $\bar{v}(r)$. Balance of the centrifugal force requires that

$$\frac{d\bar{\phi}}{dr} = \frac{1}{\bar{S}} \frac{\bar{v}^2}{r}. \quad (17)$$

Equation (17) introduces two new variables. The variable ϕ represents either the scaled density of a 2D homentropic vortex, or the geopotential of a shallow-water vortex; that is,

$$\phi \equiv \begin{cases} \frac{c_o^2}{\rho_o} \rho & \text{2D homentropic gas model,} \\ gh & \text{shallow-water model.} \end{cases} \quad (18)$$

In both cases, ϕ has units of velocity squared. The second variable \bar{S} is defined by

$$\bar{S} \equiv \begin{cases} \frac{\bar{c}^2}{\bar{\rho}} \frac{\rho_o}{c_o^2} & \text{2D homentropic gas model,} \\ 1 & \text{shallow-water model.} \end{cases} \quad (19)$$

The above definition of \bar{S} involves the squared equilibrium sound speed,

$$\bar{c}^2 \equiv \left(\frac{\partial p}{\partial \rho} \right) = \frac{c_o^2}{\rho_o^{\gamma-1}} \bar{\rho}^{\gamma-1}, \quad (20)$$

in which the derivative is evaluated at constant entropy, and γ is the ratio of specific heats (C_p/C_v).

Small perturbations about the equilibrium are governed by three linear equations. The radial and azimuthal velocity perturbations u' and v' are governed by

$$\left(\frac{\partial}{\partial t} + \bar{\Omega} \frac{\partial}{\partial \varphi} \right) u' = 2\bar{\Omega} v' - \frac{\partial}{\partial r} \phi'_s \quad (21)$$

and

$$\left(\frac{\partial}{\partial t} + \bar{\Omega} \frac{\partial}{\partial \varphi} \right) v' = -\bar{\zeta} u' - \frac{1}{r} \frac{\partial}{\partial \varphi} \phi'_s. \quad (22)$$

Here, we have introduced the equilibrium angular rotation frequency $\bar{\Omega}(r) \equiv \bar{v}/r$, and the equilibrium vorticity profile $\bar{\zeta}(r) \equiv r^{-1} \partial(r\bar{v})/\partial r$. In addition, we have introduced ϕ'_s , which is defined by

$$\phi'_s \equiv \bar{S} \phi'. \quad (23)$$

The system is closed by the mass continuity equation

$$\left(\frac{\partial}{\partial t} + \bar{\Omega} \frac{\partial}{\partial \varphi} \right) \phi'_s = -\bar{S} \left[\frac{1}{r} \frac{\partial}{\partial r} (r \bar{\phi} u') + \frac{1}{r} \frac{\partial}{\partial \varphi} (\bar{\phi} v') \right]. \quad (24)$$

Evidently, the \bar{S} factor is the difference between the perturbation dynamics of a 2D homentropic vortex and a shallow-water vortex. If $\gamma = 2$ then $\bar{S} = 1$, and the equations [(17), (21), (22), (24)] governing both systems are identical. For arbitrary γ , the value of \bar{S} is unity only in the radiation zone.

Because the 2D homentropic vortex is so closely related to the shallow-water vortex, the analytical equations of section 2b and 2c for acoustic radiation are easily converted into equations for gravity wave radiation from a shallow-water vortex (cf. Ford 1994a). One need only make the substitutions

$$\begin{aligned} \frac{p'}{\rho_o} &\rightarrow gh', & c_o &\rightarrow c_g \equiv \sqrt{gh(\infty)}, \\ M &\rightarrow \text{Fr} \equiv \frac{V}{c_g}, \end{aligned} \quad (25)$$

in which Fr is the rotational Froude number, and p' denotes either p_n or p_N . For the problem of corotating vortices, $V = \Omega_N R$.

Before proceeding, we note that the velocity Eqs. (21) and (22) neglect the Coriolis force, since it is not very important for the problem of tornado infrasound. On the other hand, we must point out that the Coriolis force causes a low-frequency cutoff (the Coriolis pa-

parameter) for gravity wave radiation from an atmospheric vortex.

b. The wave equation

The wave equation is obtained from (21), (22), and (24) by assuming a perturbation of the form

$$\phi'_s \propto \Phi(r)e^{i(n\varphi - \nu t)} + \text{cc}, \tag{26}$$

and likewise for the velocity fields.⁵ The result is

$$\begin{aligned} \frac{1}{r} \frac{d}{dr} \left(\frac{r\bar{\phi}}{2\bar{\zeta}\bar{\Omega} - \sigma^2} \frac{d\Phi}{dr} \right) - \frac{n}{r\sigma} \frac{d}{dr} \left(\frac{2\bar{\Omega}\bar{\phi}}{2\bar{\zeta}\bar{\Omega} - \sigma^2} \right) \Phi \\ - \left[\frac{n^2\bar{\phi}}{r^2(2\bar{\zeta}\bar{\Omega} - \sigma^2)} + \frac{1}{S} \right] \Phi = 0, \end{aligned} \tag{27}$$

in which

$$\sigma(r) = \nu - n\bar{\Omega} \tag{28}$$

is the ‘‘Doppler shifted’’ wave frequency. Acceptable values of the complex wave frequency ν (eigenvalues) are restricted by a regularity condition on Φ at the origin and a radiation condition on Φ at infinity. Discrete vortex Rossby waves, coupled to outer spiral acoustic/gravity waves, form one class of possible solutions.

c. Potential vorticity and angular pseudomomentum

Potential vorticity is a useful concept for discussing the dynamics of both 2D homentropic vortices and shallow-water vortices. It is here defined by

$$q \equiv \frac{\zeta}{\phi}, \tag{29}$$

and is conserved along material trajectories. The linearized equation for the potential vorticity perturbation is given by

$$\left(\frac{\partial}{\partial t} + \bar{\Omega} \frac{\partial}{\partial \varphi} \right) q' = -u' \frac{d\bar{q}}{dr}. \tag{30}$$

For the remainder of this section, we restrict our attention to monotonic vortices for which $d\bar{q}/dr < 0$ everywhere.

Another convenient variable for analyzing spontaneous acoustic/gravity wave radiation is the angular pseudomomentum,

$$\mathcal{L} \equiv - \frac{r\bar{\phi}^2 (q')^2}{2d\bar{q}/dr} - \frac{rv'\phi'_s}{S}. \tag{31}$$

⁵ As usual, cc denotes the complex conjugate of the preceding term.

The angular pseudomomentum is useful because it is quadratic in the perturbation fields and satisfies a relatively simple flux-conservation law:

$$\frac{\partial \mathcal{L}}{\partial t} = -\nabla \cdot \mathcal{F}, \tag{32}$$

in which

$$\mathcal{F} = -r\bar{\phi}u'v'\hat{\mathbf{r}} + \left\{ r\bar{\Omega}\mathcal{L} - \frac{r\bar{\phi}}{2} [(v')^2 - (u')^2] - \frac{r(\phi'_s)^2}{2S} \right\} \hat{\boldsymbol{\phi}}. \tag{33}$$

One may readily verify that Eq. (32) follows directly from the linearized equations of motion. A conservation law for nonlinear perturbations also exists, but is not pertinent to our discussion (Guinn and Schubert 1993; Schechter and Montgomery 2006).

d. Growth rate of a radiative vortex Rossby wave

In the context of the shallow-water problem, Eq. (32) has been converted into an equation for the amplitude a of a radiative vortex Rossby wave near marginal stability (Schechter and Montgomery 2006). The result is an equation of the form

$$\frac{da}{dt} = (\nu_{\text{rad}} - \nu_{\text{cl}})a. \tag{34}$$

The first term ν_{rad} of the growth rate accounts for the positive feedback of the radiation. The second term $-\nu_{\text{cl}}$ accounts for the negative feedback of a resonant disturbance of potential vorticity at a critical radius r_* . The critical radius is defined implicitly by

$$n\bar{\Omega}(r_*) = \omega, \tag{35}$$

in which n is the azimuthal wavenumber of the Rossby wave and ω is the oscillation frequency. It is where the angular rotation frequency of the vortex equals the angular phase velocity of the wave. In general, a Rossby wave critical radius r_* is outside the vortex core.

The explicit formula for the radiative pumping rate is given by

$$\nu_{\text{rad}} = \frac{r^2\bar{\phi}\Re[UV^*]}{I} \Big|_{r=r_e}, \tag{36}$$

in which $\Re[. . .]$ is the real part of the quantity in square brackets, and r_e is located at the beginning of the radiation zone. The variables $U(r)$ and $V(r)$ are the radial and azimuthal velocity wave functions. The superscript $*$ is the complex conjugate operator. The denominator I is given by

$$I = - \int_0^{r_e} dr \left\{ \frac{r^2 \bar{\phi}^2 |U|^2 d\bar{q}}{|\omega - n\bar{\Omega}|^2 dr} + 2 \frac{r^2 \Re[V\Phi^*]}{\bar{S}} \right\}, \quad (37)$$

in which the fractured integral f excludes a thin layer centered at r_* . The value of I is generally positive for vortex Rossby wave perturbations in a monotonic vortex.

The explicit formula for the critical-layer damping rate is given by

$$\nu_{cl} = - \frac{\pi r^2 \bar{\phi}^2 |U|^2 d\bar{q}/dr}{I n |d\bar{\Omega}/dr|} \Big|_{r=r_*}. \quad (38)$$

Since the radial gradient of \bar{q} is negative, ν_{cl} is positive. If the magnitude of $d\bar{q}/dr$ exceeds a threshold at r_* , the critical-layer damping term will dominate the radiative pumping term in Eq. (34).

In general, the growth rate $\nu_{tot} = \nu_{rad} - \nu_{cl}$ cannot be reduced to closed form. One notable exception is for the Rossby waves of a modified Rankine vortex at Mach numbers (Froude numbers) much less than unity. The modification is a skirt of very small potential vorticity that extends beyond the core radius R and contains all critical layers. We may treat this skirt as a very small perturbation to the basic state. In doing so, the analysis yields

$$\nu_{tot} = \frac{\pi n(n-1)^{2n}}{(n!)^2 2^{2n}} M^{2n} \Omega + \frac{\pi}{4n} \left(\frac{n-1}{n} \right)^{n-3/2} c_o^2 R \frac{d\bar{q}}{dr_*}, \quad (39)$$

in which the first and second terms correspond to ν_{rad} (cf. Kop'ev and Leont'ev 1983) and $-\nu_{cl}$ (cf. Briggs et al. 1970), respectively.⁶ Appendix B contains details of the derivation, and the formula for $r_*(n)$ [Eq. (B18)]. For the shallow-water vortex, one should replace c_o with c_g and M with Fr . The above expression does not include finite Mach number corrections to ν_{cl} . These corrections are quantitatively important only when ν_{tot} is much smaller than the individual terms on the right-hand side of Eq. (39).

e. Nonlinear effects

Of course, linear theory has limitations. Any damped vortex Rossby wave will survive if the magnitude of its initial wave activity exceeds the absorption capacity of its critical layer (Briggs et al. 1970; Pillai and Gould 1994; Schecter et al. 2000; Balmforth et al. 2001). Once

the critical layer saturates, the positive feedback of radiative pumping tends to prevail (Schecter and Montgomery 2006). The amplitude that is required for survival (and revival) increases with the negative potential vorticity gradient at r_* .

In general, r_* is located beyond the radius of maximum wind. Therefore, as in linear theory, vortices with steep potential vorticity gradients outside their cores are less likely to sustain their Rossby waves (cf. Chan et al. 1993). In contrast, nearly Rankine vortices are likely to sustain their Rossby waves, so long as eddy diffusion is negligible.

f. Nonmodal perturbations

Nonmodal perturbations, or sheared vortex Rossby waves (Montgomery and Kallenbach 1997), may also contribute significantly to the production of spiral infrasound. Such perturbations can exhibit transient growth (Nolan and Farrell 1999) and thereby amplify the radiation field. However, their pressure fields are expected to decay algebraically as time goes to infinity (e.g., Bassom and Gilbert 1998; Brunet and Montgomery 2002).

7. Concluding remarks

For convenient reference, Table 5 lists some notable results that were either reviewed or discovered in this paper.

To begin with, this paper reviewed the basic theory of the adiabatic generation of spiral infrasound by tornado-like vortices. The spiral infrasound of a tornado-like vortex is created by various means. Here, we focused on the following two sources:

- (i) vortex Rossby waves and
- (ii) corotating suction vortices.

In both cases, the frequency of the infrasound increases with the azimuthal wavenumber (n or N) of the source. Moreover, the intensity of the infrasound rapidly amplifies with increasing Mach number or decreasing wavenumber. However, it is important to reiterate that eddy viscosity or critical layers in a monotonic vortex can strongly damp its Rossby waves, and thereby inhibit the production of infrasound.

To gain perspective, we used RAMS to simulate the infrasound of a disorganized nontornadic thunderstorm, a few kilometers wide. In this simulation, the dominant component of the 0.1–10-Hz infrasound seemed to radiate from the vicinity of the melting level, where diabatic processes involving hail were active. We showed that the 3D vortex Rossby waves of an F2–F5

⁶ Note that d/dr_* is shorthand for the radial derivative evaluated at r_* .

TABLE 5. Summary and key remarks.

Topic	Text/figures/tables	Remarks
3D Lighthill radiation from compact adiabatic turbulence	Sections 2a and 5/Fig. 19	May contribute significantly to the 0.1–10-Hz infrasound of a thunderstorm if the turbulence has a characteristic frequency between 0.1 and 10 Hz and a Mach number no less than 0.1.
Analytical theory of a 2D Rankine vortex	Section 2b, appendixes A and B/Figs. 1 and 2/Table 1	The amplitudes of the emitted spiral waves decrease as n increases and as V decreases.
Analytical theory of a 2D ring of corotating vortices	Section 2c, appendix A/Figs. 3 and 4/Table 2	The amplitudes of the emitted spiral waves decrease as N increases and as V decreases.
RAMS simulations of a 2D Rankine vortex	Section 3a, appendixes C and D/Figs. 5 and 6/Table 1	Radiation amplitudes agree with analytical results at wave Mach numbers < 0.2 .
RAMS sensitivity to dissipation parameters	Section 3b, appendix C2/Fig. 7	As diffusive eddy fluxes increase toward values that are common to present-day thunderstorm simulations, the vortex rapidly symmetrizes and its radiation is damped.
RAMS simulations of a 2D ring of corotating vortices	Section 3c, appendixes C and D2/Figs. 8 and 9/Table 2	Radiation amplitudes agree with analytical results at Mach numbers < 0.1 .
RAMS simulations of a vertically sheared Rankine vortex	Sections 3d and 5, appendix D1/Figs. 10–12 and 18	3D vortex Rossby waves of modest amplitude can produce infrasound that dominates the acoustic radiation of a simulated nontornadic thunderstorm at frequencies of order 0.1 Hz.
RAMS simulation of a nontornadic thunderstorm in a shear-free environment	Sections 4 and 5, appendix C/ Figs. 13–18/Tables 3 and 4	The pertinent infrasound appears to radiate from the vicinity of the melting level, where diabatic processes involving hail are active. The barely resolved 0.5–2.5-Hz infrasound is an order of magnitude lower than the corresponding infrasound that is observed from severe weather. Also see above.
Critical layers	Section 6, appendix B/Fig. 20	Critical layers within a smooth monotonic vortex tend to inhibit spiral acoustic radiation.

tornado-like vortex, with a 200-m diameter, can freely emit spiral acoustic waves of greater magnitude than the 0.1–10-Hz thunderstorm noise. This seminal result will require future verification, using thunderstorm models that have different parameterizations of microphysical processes. However, we expect that the infrasound of strong tornadoes will remain dominant.

Of course, real tornadoes are more complex than the vortices considered here. For example, a tornado can have an irregular serpentine geometry. More generally, a tornado will have an evolving mean flow with secondary circulation and clouds. This situation may encourage axisymmetric vibrations and diabatic turbulence aloft. Such features may create 0.1–10-Hz infrasound at or above the level that is produced by vortex Rossby waves or corotating suction vortices. Thus, we have not yet resolved the prevailing source of tornado infrasound.

In principle, the best way to numerically study tornado infrasound is to analyze full physics simulations of tornadic supercells. The results of this paper suggest that reliable (converged) results may require 1-m grid spacing in the region of the tornado. Perhaps the best strategy is to develop a compressible adaptive grid model that efficiently resolves small-scale fluctuations in a moving, bending vortex. Clearly, the problem of

tornado infrasound opens a new frontier of atmospheric modeling.

Acknowledgments. The authors thank Dr. Stephen Saleeby for helpful discussions regarding RAMS. This work was supported in part by NSF Grant ATM-0347478.

APPENDIX A

Matching Vortex Flow to the Radiation Field

In this appendix, we derive formulas for the spiral radiation fields that are generated by the Rossby waves of a 2D Rankine vortex [Eq. (5)] and by a ring of N corotating point vortices [Eq. (11)]. The derivations sacrifice rigor for brevity. Nevertheless, the end results are consistent with those found in, say, Howe (1975, 2003), Broadbent (1976), Kop'ev and Leont'ev (1983), Lyamshev and Skvortsov (1988), and Aurégan et al. (2002).

a. The vortex flow

At low Mach numbers, we may regard the flow in the vortex region, $r \ll \lambda \sim R/M$, as divergence free. Accordingly, the vortex velocity field is approximately the cross gradient of a streamfunction; that is,

$$(u, v) = \left(-\frac{1}{r} \frac{\partial \psi}{\partial \varphi}, \frac{\partial \psi}{\partial r} \right). \quad (\text{A1})$$

From Eq. (A1), the vorticity is given by

$$\zeta = \frac{1}{r} \frac{\partial}{\partial r} \left(r \frac{\partial \psi}{\partial r} \right) + \frac{1}{r^2} \frac{\partial^2 \psi}{\partial \varphi^2}. \quad (\text{A2})$$

The vortex motion is completely determined by the equation

$$\frac{\partial \zeta}{\partial t} - \frac{1}{r} \frac{\partial \psi}{\partial \varphi} \frac{\partial \zeta}{\partial r} + \frac{1}{r} \frac{\partial \psi}{\partial r} \frac{\partial \zeta}{\partial \varphi} = 0, \quad (\text{A3})$$

and the boundary condition that the velocity field [Eq. (A1)] asymptotically decays toward zero as $r \rightarrow \infty$ (as r approaches the radiation zone). The pressure field does not appear in the above dynamical formulation; however, we will relate it to ψ when the time comes.

In general, we may expand the flow in a Fourier series in the azimuthal coordinate φ ; that is,

$$\psi(r, \varphi, t) = \psi_0(r, t) + \sum_{n=1}^{\infty} [\psi_n(r, t) e^{in\varphi} + \text{cc}], \quad (\text{A4})$$

and likewise for all other flow variables. For a Rankine vortex with Rossby waves propagating along its boundary, we have, to first order in the perturbation amplitude,

$$\psi_0 = \begin{cases} \frac{\Omega(r^2 - R^2)}{2} & r \leq R, \\ \Omega R^2 \ln\left(\frac{r}{R}\right) & r > R, \end{cases}$$

$$\psi_n = -\epsilon_n \frac{\Omega R^2}{2n} \left(\frac{r_{<}}{r_{>}} \right)^n e^{-i\omega_n t}, \quad (\text{A5})$$

in which $r_{<}$ ($r_{>}$) is the lesser (greater) of r and R , and ϵ_n is a dimensionless complex constant. For a rigid ring of N corotating point vortices, we have

$$\psi_0 = \frac{\Gamma N}{2\pi} \ln\left(\frac{r_{>}}{R}\right),$$

$$\psi_n = -\alpha_n \frac{\Gamma N}{4\pi n} \left(\frac{r_{<}}{r_{>}} \right)^n e^{-in\Omega_N t}, \quad (\text{A6})$$

in which α_n is unity (zero) if n equals (does not equal) an integral multiple of N .

The harmonics in Eqs. (A5) and (A6) each have the form

$$\psi_n(r, t) = \Psi_n(r) e^{-iv_n t}, \quad (\text{A7})$$

in which

$$v_n = \begin{cases} \omega_n & \text{Rankine vortex,} \\ n\Omega_N & \text{corotating vortices.} \end{cases} \quad (\text{A8})$$

For later convenience, we here define the Doppler-shifted frequency,

$$\sigma_n(r) \equiv v_n - n\bar{\Omega}(r), \quad (\text{A9})$$

in which $\bar{\Omega} = r^{-1} d\psi_0/dr$.

Although we merely cited the vortex Rossby wave solutions, they were derived under the assumption that linear theory is valid everywhere. For $r \gg R$, the waves generated by the point vortex ring should also satisfy linearized equations. In the region where linear theory applies, the density variable will have the form

$$\phi_s' = \sum_{n=1}^{\infty} [\Phi_n(r) e^{i(n\varphi - v_n t)} + \text{cc}], \quad (\text{A10})$$

in which from Eq. (22),

$$\Phi_n = \sigma_n \frac{r}{n} \frac{d\Psi_n}{dr} + \bar{\zeta} \Psi_n. \quad (\text{A11})$$

For Rossby waves on a Rankine vortex, this formula yields

$$\Phi_n = \begin{cases} -\frac{\epsilon_n R^2 \Omega^2}{2n} \left(\frac{r}{R} \right)^n, & r < R, \\ \frac{\epsilon_n R^2 \Omega^2}{2n} \left(\frac{R}{r} \right)^n \left[n - 1 - n \left(\frac{R}{r} \right)^2 \right], & r > R. \end{cases} \quad (\text{A12})$$

For a ring of N corotating point vortices, we have

$$\Phi_n = \alpha_n \left(\frac{\Gamma}{4\pi} \right)^2 \frac{N(N-1)}{R^2} \left(\frac{R}{r} \right)^n, \quad r \gg R. \quad (\text{A13})$$

b. The radiation field

In the radiation zone, the $n = 0$ component of the vortex velocity field is negligible, and \bar{S} is unity. Moreover, the general solution of the wave equation [(27)] approximately has the form

$$\Phi_n = a_n H_n^{(1)}(\kappa) + b_n H_n^{(2)}(\kappa), \quad (\text{A14})$$

in which a_n and b_n are complex constants, $H_n^{(i)}$ is a Hankel function of the i th kind, and

$$\kappa \equiv \frac{v_n}{c_o} r. \quad (\text{A15})$$

Since there are no inward propagating waves, $b_n = 0$. The asymptotic forms of the Hankel function of the first kind are (e.g., Abramowitz and Stegun 1972)

$$H_n^{(1)}(\kappa) \sim \begin{cases} -\frac{i2^n(n-1)!}{\pi\kappa^n} & \kappa \ll 1, \\ \sqrt{\frac{2}{\pi\kappa}} e^{i[\kappa - (2n+1)\pi/4]} & \kappa \gg 1. \end{cases} \quad (\text{A16})$$

To obtain the complex amplitude a_n , we simply match the inner ($\kappa \ll 1$) radiation field to the outer ($r \gg R$) vortex field. The result is

$$a_n = \begin{cases} \frac{i\pi\epsilon_n(n-1)^{n+1}(R\Omega)^{n+2}}{n!2^{n+1}c_o^n} & \text{Rankine vortex,} \\ \frac{i\pi\alpha_n n^n N(R\Omega_n)^{n+2}}{(N-1)(n-1)!2^n c_o^n} & \text{corotating vortices.} \end{cases} \quad (\text{A17})$$

Substituting Eqs. (A17) and $b_n = 0$ into Eq. (A14) and assuming $\kappa \gg 1$ leads to Eqs. (5) and (11) of the main text.

APPENDIX B

Growth Rate of a 2D Vortex Rossby Wave

The general formula for the growth rate of a nearly neutral 2D vortex Rossby wave is given by (cf. section 6d)

$$v_{\text{tot}} = v_{\text{rad}} - v_{\text{cl}}, \quad (\text{B1})$$

in which

$$v_{\text{rad}} = \frac{r^2 \bar{\phi} \Re[U_n V_n^*]}{I} \Big|_{r=r_e} \quad (\text{B2})$$

and

$$v_{\text{cl}} = -\frac{\pi r^2 \bar{\phi}^2 |U_n|^2 d\bar{q}/dr}{I n |d\bar{\Omega}/dr|} \Big|_{r=r_*}. \quad (\text{B3})$$

We may write the integral I as the sum of two parts:

$$I \equiv I_1 + I_2, \quad (\text{B4})$$

in which

$$I_1 \equiv -\int_0^{r_e} dr \frac{r^2 \bar{\phi}^2 |U_n|^2 d\bar{q}}{|\sigma_n|^2 dr} \quad (\text{B5})$$

and

$$I_2 \equiv -\int_0^{r_e} dr \frac{2r^2 \Re[V_n \Phi_n^*]}{S}. \quad (\text{B6})$$

In this appendix, we evaluate Eq. (B1) for the Rossby waves of a nearly Rankine vortex at low Mach number. Our evaluation draws upon the results of appendix A.

The first step in evaluating the right-hand side of Eq.

(B1) is to choose a proper value for the radius r_e . We will assume that

$$\frac{c_o}{v_n} \ll r_e \ll \frac{c_o}{v_{\text{tot}}}. \quad (\text{B7})$$

The first inequality puts r_e in the far-field ($\kappa \gg 1$). The second inequality is required because the approximation of real κ in our Hankel function solution of the acoustic radiation [Eq. (A14)] becomes inaccurate at radii greater than c_o/v_{tot} .

The next step is to evaluate the integrals I_1 and I_2 . To evaluate I_1 , we make the approximations

$$\frac{d\bar{q}}{dr} = -\frac{2\Omega}{c_o^2} \delta(r - R), \quad (\text{B8})$$

$$\sigma_n = \Omega(n-1) - n \begin{cases} \Omega & r < R, \\ \Omega \left(\frac{R}{r}\right)^2 & r > R, \end{cases} \quad (\text{B9})$$

and

$$\bar{\phi} = c_o^2. \quad (\text{B10})$$

The errors are small under the assumptions that (i) $M \ll 1$ and (ii) the vorticity distribution differs only slightly from a Rankine profile. Since the weight function $d\bar{q}/dr$ is here approximated by Eq. (B8), we may also use the inner radial wave function

$$U_n = -\frac{in}{r} \Psi_n = \frac{i\Omega R^2 \epsilon_n}{2r} \left(\frac{r_{<}}{r_{>}}\right)^n, \quad (\text{B11})$$

in which $r_{<}$ ($r_{>}$) is the lesser (greater) of r and R . Substituting Eqs. (B8)–(B11) into the right-hand side of (B5) yields

$$I_1 = \frac{|\epsilon_n|^2 R^3 c_o^3}{2} M. \quad (\text{B12})$$

It can be shown by straightforward but tedious analysis that I_2 is comparatively small for $M \ll 1$; therefore, it is here neglected.

To evaluate the numerator in Eq. (B2) for v_{rad} we may use the far-field ($\kappa \gg 1$) relations

$$U_n = \frac{\Phi_n}{c_o} \quad \text{and} \quad V_n = \frac{n}{\omega_n r} \Phi_n, \quad (\text{B13})$$

in which

$$\Phi_n = a_n \sqrt{\frac{2}{\pi\kappa}} e^{i[\kappa - (2n+1)\pi/4]} \quad (\text{B14})$$

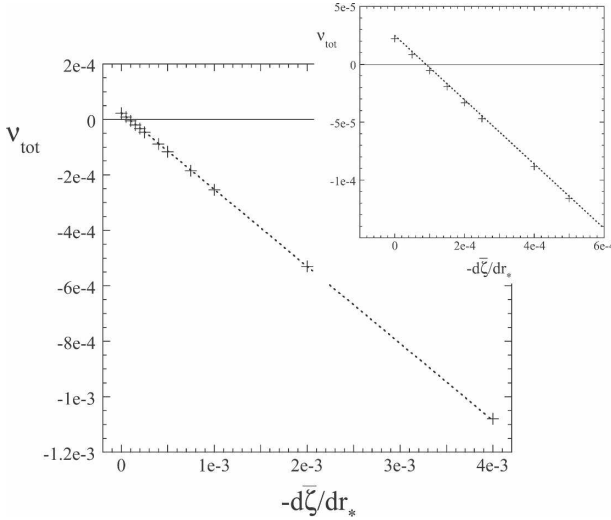


FIG. B1. Growth rate of the $n = 2$ Rossby wave of a 2D homentropic Rankine-with-skirt vortex at $M = 0.15$. The + symbols are from numerical solutions of the vortex eigenmode problem, generalized to find exponentially damped quasi modes. The dotted line is Eq. (39). The inset is a blowup of the region where radiative pumping is comparable to critical-layer damping. The growth rate ν_{tot} is normalized to 2Ω . The critical-layer vorticity gradient $d\bar{\zeta}/dr_*$ is normalized to $2\Omega/R$. At low Mach numbers, $d\bar{\zeta}/dr_* \approx c_o^2 d\bar{q}/dr_*$.

and a_n is given by Eq. (A17). The result is

$$r^2 \bar{\phi} \Re[U_n V_n^*]|_{r=r_e} = \frac{\pi |\epsilon_n|^2 R^2 c_o^4 n(n-1)^{2n}}{(n!)^2 2^{2n+1}} M^{2n+2}. \quad (\text{B15})$$

Dividing Eq. (B15) by (B12) leads to

$$\nu_{\text{rad}} = \frac{\pi n(n-1)^{2n}}{(n!)^2 2^{2n}} M^{2n} \Omega. \quad (\text{B16})$$

To evaluate the resonant factor in Eq. (B3) for ν_{cl} , we may use Eq. (B11) for U_n and Eq. (B10) for $\bar{\phi}$. Furthermore, we may use the approximations

$$\frac{d\bar{\Omega}}{dr} = -\frac{2\Omega R^2}{r^3}, \quad r > R \quad (\text{B17})$$

and

$$r_* = R \sqrt{\frac{n}{n-1}}. \quad (\text{B18})$$

The end result is

$$\nu_{\text{cl}} = -\frac{\pi}{4n} \left(\frac{n-1}{n}\right)^{n-3/2} c_o^2 R \frac{d\bar{q}}{dr_*}. \quad (\text{B19})$$

Subtracting Eq. (B19) from Eq. (B16) gives Eq. (39) of the main text for ν_{tot} . Because of the large number of

approximations that were based more on physical intuition than mathematical rigor, it is important to check the validity of Eq. (39). Figure B1 shows by example that there is good agreement between the analytical growth rate formula and numerical solutions of the eigenmode problem, generalized to compute exponentially damped quasi modes (cf. Spencer and Rasband 1997; Schecter et al. 2000, 2002; Schecter and Montgomery 2004, 2006).

APPENDIX C

RAMS Configuration for the Vortex Sound Simulations

a. The dry core

For this paper, the dry core of RAMS was slightly improved from its standard form, as in Medvigy et al. (2005). Let \mathbf{v} represent the three-dimensional velocity field. In addition, let

$$\Pi \equiv c_{pd} \left(\frac{p}{p_r}\right)^{R_d/c_{pd}}, \quad (\text{C1})$$

in which $p_r = 10^5$ Pa is a reference pressure, R_d is the gas constant of dry air, and c_{pd} is the specific heat of dry air at constant pressure. Finally, let

$$\theta \equiv \frac{c_{pd} T}{\Pi} \quad (\text{C2})$$

denote the potential temperature. The basic state of the atmosphere is here assumed to be at rest, with $\theta = \theta_o(z)$, $\Pi = \Pi_o(z)$, and $\rho = \rho_o(z)$.

Neglecting the Coriolis force, the velocity equation is

$$\frac{\partial \mathbf{v}}{\partial t} + \mathbf{v} \cdot \nabla \mathbf{v} + \theta_o \nabla \Pi' = g \frac{\theta'}{\theta_o} \hat{\mathbf{z}} + \text{Turb}(\mathbf{v}), \quad (\text{C3})$$

in which primes here denote perturbations about the rest state of the atmosphere, g is gravitational acceleration, and Turb is nominally a tendency due to subgrid-scale turbulence. The adiabatic heat equation is

$$\frac{\partial \theta}{\partial t} + \mathbf{v} \cdot \nabla \theta = \text{Turb}(\theta). \quad (\text{C4})$$

The Π' equation, which substitutes for mass continuity, is

$$\frac{\partial \Pi'}{\partial t} + \frac{c_o^2}{\theta_o^2 \rho_o} \nabla \cdot (\mathbf{v} \rho_o \theta_o) = -\mathbf{v} \cdot \nabla \Pi' - \frac{R_d \Pi'}{c_{vd}} \nabla \cdot \mathbf{v} + \frac{c^2 d\theta}{\theta^2 dt}, \quad (\text{C5})$$

in which c_{vd} is the specific heat of dry air at constant volume, $c^2 = (\partial p / \partial \rho)_\theta = c_{pd} R T / c_{vd}$ is the squared atmo-

spheric sound speed, and $c_o^2(z)$ represents c^2 for the rest state. The right-hand side of Eq. (C5) is neglected in standard RAMS.

It is important to mention that the velocity equation is inexact, in that θ_o as opposed to θ multiplies the gradient of Π' . However, if θ_o is constant and θ' is initially zero, then $\theta = \theta_o$ and $\theta' = 0$ for all time. That is, the equations are exact for the special case of homentropic initial conditions.

b. Dissipation

The dissipation terms are here used for numerical stability. However, their functional forms come from a standard K -theory parameterization of subgrid-scale turbulence. Specifically,

$$\text{Turb}(v_j) \equiv \sum_{i=1}^3 \frac{\partial}{\partial x_i} \left[K_{mi} \left(\frac{\partial v_i}{\partial x_j} + \frac{\partial v_j}{\partial x_i} \right) \right] \quad (C6)$$

and

$$\text{Turb}(\theta) \equiv \sum_{i=1}^3 \frac{\partial}{\partial x_i} \left(K_{hi} \frac{\partial \theta}{\partial x_i} \right), \quad (C7)$$

in which the i (or j) indicates the horizontal ($i = 1, 2$) and vertical ($i = 3$) components of the subscripted variable.

The mixing coefficients K_{mi} and K_{hi} are not constants; rather,

$$K_{mi} \equiv (C_x \Delta x)(C_z \Delta z) \left[D + \sqrt{\max(-N^2, 0)} \right] \times \sqrt{\max(0, 1 - R_{hm} Ri)} H(0.25 - Ri) \quad (C8)$$

and

$$K_{hi} = R_{hm} K_{mi}. \quad (C9)$$

Here, Δx is the horizontal grid spacing and Δz is the vertical grid spacing. Both C_x and C_z are user-defined dimensionless constants. The Heaviside step-function $H(x)$ is unity for $x > 0$ and is zero otherwise. The local static stability is defined by

$$N^2 \equiv \frac{g}{\theta} \frac{\partial \theta}{\partial z}, \quad (C10)$$

and the Richardson number by

$$Ri \equiv \frac{N^2}{D^2}. \quad (C11)$$

The local deformation rate is here defined by

$$D \equiv \sqrt{\sum_{i,j} \left(\frac{\partial v_i}{\partial x_j} + \frac{\partial v_j}{\partial x_i} \right)^2}. \quad (C12)$$

Finally R_{hm} is the user-defined ratio between the θ and velocity mixing coefficients.

c. Boundary conditions

The lateral boundaries permit outward-propagating acoustic radiation via the Klemp–Wilhelmson scheme, with the wave speed c_* set equal to the atmospheric sound speed (Klemp and Wilhelmson 1978). The top boundary is a rigid wall ($w = 0$) with free slip; a Rayleigh friction layer is optionally imposed. Surface fluxes of momentum and θ are all set equal to zero.

APPENDIX D

Vortex Initialization

a. 2D and 3D Rankine vortices

In general, the quasi Rankine vortices of sections 3a and 3d are initialized with no vertical velocity, no horizontal divergence, and vertical vorticity distributions of the form

$$\zeta \equiv \hat{\mathbf{z}} \cdot \nabla \times \mathbf{v}_h = Z_o e^{-z/h_z} \left[H(r_v - r) + \frac{1}{1 - (R_b/R)^2} H(r - r_v) H(R_b - r) \right]. \quad (D1)$$

Here, \mathbf{v}_h is the horizontal velocity field, h_z is a constant vertical length scale, H is the Heaviside step function, R is the vortex radius, and $R_b \gg R$. Furthermore,

$$r_v(\varphi) = R + \delta \cos(n\varphi) - \frac{\delta^2}{4R}, \quad (D2)$$

in which $\delta \ll R$ measures the radial deformation of the vortex boundary. Note that ζ includes a halo of low negative vorticity that ensures roughly zero circulation beyond the radius R_b . This halo reduces wave generation at the square domain boundary.

Because $\nabla \cdot \mathbf{v}_h = 0$, we may write

$$\mathbf{v}_h = \hat{\mathbf{z}} \times \nabla \psi \quad (D3)$$

and

$$\frac{\partial^2 \psi}{\partial x^2} + \frac{\partial^2 \psi}{\partial y^2} = \zeta. \quad (D4)$$

It is assumed that $\psi = 0$ on the lateral boundaries of the square simulation domain.

The Π' field is determined by the additional constraint

$$\frac{\partial}{\partial t} \nabla \cdot \mathbf{v}_h = 0 \quad (D5)$$

at $t = 0$. Equation (D5) in combination with the divergence of the horizontal velocity equation implies that

$$\frac{\partial^2 \Pi'}{\partial x^2} + \frac{\partial^2 \Pi'}{\partial y^2} = \frac{2}{\theta_o} \left[\frac{\partial^2 \psi}{\partial x^2} \frac{\partial^2 \psi}{\partial y^2} - \left(\frac{\partial^2 \psi}{\partial x \partial y} \right)^2 \right]. \quad (D6)$$

It is assumed that $\Pi' = 0$ on the lateral boundaries of the square simulation domain.

The θ' field is determined by hydrostatic balance ($dw/dt = 0$). The result is

$$\theta' = \frac{\theta_o^2}{g} \frac{\partial \Pi'}{\partial z}. \quad (\text{D7})$$

Equations (D4), (D6), and (D7) are solved sequentially for the basic state of the vortex.

The 2D homentropic vortex of section 3a has infinite h_z , constant θ_o , and zero θ' .

b. 2D ring of N corotating vortices

In section 3c, we examined the infrasound that is radiated by a 2D ring of N corotating suction vortices in a homentropic atmosphere. Each ring has an initial vertical vorticity distribution of the form

$$\zeta(r, \varphi) = \frac{4\Gamma}{\pi d^2} \sum_{j=1}^N H[r^2 + R^2 - 2rR \cos(\varphi - 2\pi j/N) - (d/2)^2], \quad (\text{D8})$$

in which R is the ring radius and d is the diameter of an individual suction vortex.

As before, \mathbf{v}_h is initially determined by Eqs. (D3) and (D4). Furthermore, Π' is initially determined by Eq. (D6). Since the atmosphere is homentropic, θ_o is constant and θ' is zero.

REFERENCES

- Abdullah, A. J., 1966: The “musical” sound emitted by a tornado. *Mon. Wea. Rev.*, **94**, 213–220.
- Abramowitz, M., and A. Stegun, Eds., 1972: *Handbook of Mathematical Functions with Formulas, Graphs, and Mathematical Tables*. Dover, 1046 pp.
- Aurégan, Y., A. Maurel, V. Pagneux, and J.-F. Pinton, Eds., 2002: *Sound-Flow Interactions*. Springer-Verlag, 286 pp.
- Balmforth, N. J., S. G. Lewellyn Smith, and W. R. Young, 2001: Disturbing vortices. *J. Fluid Mech.*, **426**, 95–133.
- Bassom, A. P., and A. D. Gilbert, 1998: The spiral wind-up of vorticity in an inviscid planar vortex. *J. Fluid Mech.*, **371**, 109–140.
- Bedard, A. J., Jr., 2005: Low-frequency atmospheric acoustic energy associated with vortices produced by thunderstorms. *Mon. Wea. Rev.*, **133**, 241–263.
- , W. A. Lyons, R. A. Armstrong, T. E. Nelson, B. Hill, and S. Gallagher, 1999: A search for low-frequency atmospheric acoustic waves associated with sprites, blue jets, elves and storm electrical activity. *Eos, Trans. Amer. Geophys. Union*, **80** (Fall Meeting Suppl.), F227.
- , B. W. Bartram, A. N. Keane, D. C. Welsh, and R. T. Nishiyama, 2004: The infrasound network (ISNet): Background, design details, and display capability as a 88D adjunct tornado detection tool. Preprints, *22nd Conf. on Severe Local Storms*, Hyannis, MA, Amer. Meteor. Soc., 1.1.
- Briggs, R. J., J. D. Daugherty, and R. H. Levy, 1970: Role of Landau damping in crossed-field electron beams and inviscid shear flow. *Phys. Fluids*, **13**, 421–432.
- Broadbent, E. G., 1976: Jet noise radiation from discrete vortices. Royal Aircraft Establishment Tech. Rep. 76034, 28 pp.
- Brunet, G., and M. T. Montgomery, 2002: 2002: Vortex Rossby waves on smooth circular vortices: I. Theory. *Dyn. Atmos. Oceans*, **35**, 153–177.
- Chan, W. M., K. Shariff, and T. H. Pulliam, 1993: Instabilities of two-dimensional inviscid compressible vortices. *J. Fluid Mech.*, **253**, 173–209.
- Chimonas, G., and H. M. Hauser, 1997: The transfer of angular momentum from vortices to gravity swirl waves. *J. Atmos. Sci.*, **54**, 1701–1711.
- Chow, K. C., and K. L. Chan, 2003: Angular momentum transports by moving spiral waves. *J. Atmos. Sci.*, **60**, 2004–2009.
- Church, C. R., J. T. Snow, G. L. Baker, and E. M. Agee, 1979: Characteristics of tornado-like vortices as a function of swirl ratio: A laboratory investigation. *J. Atmos. Sci.*, **36**, 1755–1776.
- Cotton, W. R., and Coauthors, 2003: RAMS 2001: Current status and future directions. *Meteor. Atmos. Phys.*, **82**, 5–29.
- Daigle, G. A., M. R. Stinson, and D. I. Havelock, 1996: Experiments on surface waves over a model impedance plane using acoustical pulses. *J. Acoust. Soc. Amer.*, **99**, 1993–2005.
- Few, A. A., 1969: Power spectrum of thunder. *J. Geophys. Res.*, **74**, 6926–6934.
- , A. J. Dessler, D. J. Latham, and M. Brook, 1967: A dominant 200 Hz peak in the acoustic spectrum of thunder. *J. Geophys. Res.*, **72**, 6149–6154.
- Fine, K. S., A. C. Cass, W. G. Flynn, and C. F. Driscoll, 1995: Relaxation of 2D turbulence to vortex crystals. *Phys. Rev. Lett.*, **75**, 3277–3280.
- Finley, C. A., W. R. Cotton, and R. A. Pielke, 2001: Numerical simulation of tornadogenesis in a high-precipitation supercell. Part I: Storm evolution and transition into a bow echo. *J. Atmos. Sci.*, **58**, 1597–1629.
- Ford, R., 1994a: The instability of an axisymmetric vortex with monotonic potential vorticity in rotating shallow water. *J. Fluid Mech.*, **280**, 303–334.
- , 1994b: The response of a rotating ellipse of uniform potential vorticity to gravity wave radiation. *Phys. Fluids*, **6**, 3694–3704.
- Gall, R. L., 1983: A linear analysis of multiple vortex phenomenon in simulated tornadoes. *J. Atmos. Sci.*, **40**, 2010–2024.
- Georges, T. M., 1976: Infrasound from convective storms. Part II: A critique of source candidates. NOAA Tech. Rep. ERL 380-WPL 49, 59 pp. [Available from the National Technical Information Service, 5285 Port Royal Rd., Springfield, VA 22161.]
- Grasso, L. D., and W. R. Cotton, 1995: Numerical simulation of a tornado vortex. *J. Atmos. Sci.*, **52**, 1192–1203.
- Guinn, T. A., and W. H. Schubert, 1993: Hurricane spiral bands. *J. Atmos. Sci.*, **50**, 3380–3403.
- Havelock, T. H., 1931: The stability of motion of rectilinear vortices in ring formation. *Philos. Mag.*, **11**, 617–633.
- Howe, M. S., 1975: Contributions to the theory of aerodynamic sound and jet noise and the theory of the flute. *J. Fluid Mech.*, **71**, 625–673.
- , 1977: Sound generation by a turbulent dipole. *J. Sound Vib.*, **51**, 451–458.
- , 1985: On the long range propagation of sound over irregular terrain. *J. Sound Vib.*, **98**, 83–94.

- , 2003: *Theory of Vortex Sound*. Cambridge University Press, 216 pp.
- Jin, D. Z., and D. H. E. Dubin, 1998: Regional maximum entropy theory for vortex crystal formation. *Phys. Rev. Lett.*, **80**, 4434–4437.
- Jones, R. M., E. S. Gu, and A. J. Bedard Jr., 2004: Infrasonic and atmospheric propagation studies using a 3-D ray trace model. Preprints, *22nd Conf. on Severe Local Storms*, Hyannis, MA, Amer. Meteor. Soc., P2.9.
- Kelvin, L., 1880: On the vibrations of a columnar vortex. *Philos. Mag.*, **10**, 155–168.
- Klemp, J. B., and R. B. Wilhelmson, 1978: The simulation of three-dimensional convective storm dynamics. *J. Atmos. Sci.*, **35**, 1070–1093.
- Kop'ev, V. F., and E. A. Leont'ev, 1983: Acoustic instability of an axial vortex. *Sov. Phys. Acoust.*, **29**, 111–115.
- , and —, 1985: Energy aspect of the acoustic instability of certain steady-state vortices. *Sov. Phys. Acoust.*, **31**, 205–207.
- , and —, 1988: Acoustic instability of planar vortex flows with circular streamlines. *Sov. Phys. Acoust.*, **34**, 276–278.
- Lewellen, D. C., W. S. Lewellen, and J. Xia, 2000: The influence of a local swirl ratio on tornado intensification near the surface. *J. Atmos. Sci.*, **57**, 527–544.
- Lighthill, M. J., 1952: On sound generated aerodynamically. I. General theory. *Proc. Roy. Soc. London*, **211A**, 564–587.
- Lyamshev, L. M., and A. T. Skvortsov, 1988: Sound radiation by localized vortices in a slightly compressible medium. *Sov. Phys. Acoust.*, **34**, 447–459.
- Medvigy, D., P. R. Moorcroft, R. Avissar, and R. L. Walko, 2005: Mass conservation and atmospheric dynamics in the Regional Atmospheric System (RAMS). *Environ. Fluid Mech.*, **5**, 109–134.
- Meecham, W. C., and G. W. Ford, 1958: Acoustic radiation from isotropic turbulence. *J. Acoust. Soc. Amer.*, **30**, 318–322.
- Montgomery, M. T., and R. J. Kallenbach, 1997: A theory of vortex Rossby-waves and its application to spiral bands and intensity changes in hurricanes. *Quart. J. Roy. Meteor. Soc.*, **123**, 435–465.
- , V. A. Vladimirov, and P. V. Denissenko, 2002: An experimental study on hurricane mesovortices. *J. Fluid Mech.*, **471**, 1–32.
- Nicholls, M. E., and R. A. Pielke Sr., 1994a: Thermal compression waves. I: Total-energy transfer. *Quart. J. Roy. Meteor. Soc.*, **120**, 305–332.
- , and —, 1994b: Thermal compression waves. II: Mass adjustment and vertical transfer of total energy. *Quart. J. Roy. Meteor. Soc.*, **120**, 333–359.
- , and —, 2000: Thermally induced compression waves and gravity waves generated by convective storms. *J. Atmos. Sci.*, **57**, 3251–3271.
- , —, and W. R. Cotton, 1991: Thermally forced gravity waves in an atmosphere at rest. *J. Atmos. Sci.*, **48**, 1869–1884.
- Nolan, D. S., and B. F. Farrell, 1999: The structure and dynamics of tornado-like vortices. *J. Atmos. Sci.*, **56**, 2908–2936.
- Passner, J. E., and J. M. Noble, 2006: Acoustic energy measured in severe storms during a field study in June 2003. U.S. Army Research Laboratory Tech. Rep. ARL-TR-3749, 42 pp.
- Pielke, R. A., J. Eastman, L. D. Grasso, J. Knowles, M. Nicholls, R. L. Walko, and X. Zeng, 1995: Atmospheric vortices. *Fluid Vortices*, S. Green, Ed., Kluwer Academic, 617–650.
- Piercy, J. E., T. F. W. Embleton, and L. C. Sutherland, 1977: Review of noise propagation in the atmosphere. *J. Acoust. Soc. Amer.*, **61**, 1403–1418.
- Pillai, S., and R. W. Gould, 1994: Damping and trapping in 2D inviscid fluids. *Phys. Rev. Lett.*, **73**, 2849–2852.
- Plougonven, R., and V. Zeitlin, 2002: Internal gravity wave emission from a pancake vortex: An example of wave-vortex interaction in strongly stratified flows. *Phys. Fluids*, **14**, 1259–1268.
- Polvani, L. M., J. C. McWilliams, M. A. Spall, and R. Ford, 1994: The coherent structures of shallow-water turbulence: Deformation-radius effects, cyclone/anticyclone asymmetry and gravity-wave generation. *Chaos*, **4**, 177–186.
- Powell, A., 1964: Theory of vortex sound. *J. Acoust. Soc. Amer.*, **36**, 177–195.
- Press, W. H., S. A. Teukolsky, W. T. Vetterling, and B. P. Flannery, 1992: *Numerical Recipes in Fortran 77: The Art of Scientific Computing*. 2nd ed. Cambridge University Press, 933 pp.
- Rotunno, R., 1978: A note on the stability of a cylindrical vortex sheet. *J. Fluid Mech.*, **87**, 761–771.
- Schechter, D. A., and M. T. Montgomery, 2004: Damping and pumping of a vortex Rossby wave in a monotonic cyclone: Critical layer stirring versus inertia-buoyancy wave emission. *Phys. Fluids*, **16**, 1334–1348.
- , and —, 2006: Conditions that inhibit the spontaneous radiation of spiral inertia-gravity waves from an intense mesoscale cyclone. *J. Atmos. Sci.*, **63**, 435–456.
- , and —, 2007: Waves in a cloudy vortex. *J. Atmos. Sci.*, **64**, 314–337.
- , D. H. E. Dubin, K. S. Fine, and C. F. Driscoll, 1999: Vortex crystals from 2D Euler flow: Experiment and simulation. *Phys. Fluids*, **11**, 905–914.
- , —, A. C. Cass, C. F. Driscoll, I. M. Lansky, and T. M. O'Neil, 2000: Inviscid damping of asymmetries on a two-dimensional vortex. *Phys. Fluids*, **12**, 2397–2412.
- , M. T. Montgomery, and P. D. Reasor, 2002: A theory for the vertical alignment of a quasigeostrophic vortex. *J. Atmos. Sci.*, **59**, 150–168.
- Spencer, R. L., and S. N. Rasband, 1997: Damped diocotron quasi-modes of nonneutral plasmas and inviscid fluids. *Phys. Plasmas*, **4**, 53–60.
- Szoke, E. J., A. J. Bedard Jr., E. Thaler, and R. Glancy, 2004: A comparison of ISNet data with radar data for tornadic and potentially tornadic storms in northeast Colorado. Preprints, *22nd Conf. on Severe Local Storms*, Hyannis, MA, Amer. Meteor. Soc., 1.2.
- Tolstoy, I., 1984: Smoothed boundary conditions, coherent low-frequency scatter, and boundary modes. *J. Acoust. Soc. Amer.*, **75**, 1–22.
- Vladimirov, V. A., and V. F. Tarasov, 1980: Formation of a system of vortex filaments in a rotating liquid. *Izv. Akad. Az. Nauk SSSR Mekh. Zhid. i Gaza*, **1**, 44–51.
- Walko, R. L., W. R. Cotton, M. P. Meyers, and J. Y. Harrington, 1995: New RAMS cloud microphysics parameterization. Part 1: The single-moment scheme. *Atmos. Res.*, **38**, 29–62.
- Ward, N. B., 1972: The exploration of certain features of tornado dynamics using a laboratory model. *J. Atmos. Sci.*, **29**, 1194–1204.
- Weske, J. R., and T. M. Rankin, 1963: Generation of secondary motions in the fields of a vortex. *Phys. Fluids*, **6**, 1397–1403.
- Wurman, J., 2002: The multiple vortex structure of a tornado. *Wea. Forecasting*, **17**, 473–505.
- Zeitlin, V., 1991: On the backreaction of acoustic radiation for distributed two-dimensional vortex structures. *Phys. Fluids*, **A**, **3**, 1677–1680.